ANNUAL REVIEWS

Annual Review of Nuclear and Particle Science

The Trojan Horse Method: A Nuclear Physics Tool for Astrophysics

Aurora Tumino,[1,2] Carlos A. Bertulani,[3] Marco La Cognata,[2] Livio Lamia,[2,4,5] Rosario Gianluca Pizzone,[2] Stefano Romano,[2,4,5] and Stefan Typel[6,7]

[1]Facoltà di Ingegneria e Architettura, Università degli Studi di Enna "Kore," 94100 Enna, Italy

[2]Laboratori Nazionali del Sud, INFN, 95123 Catania, Italy; email: tumino@lns.infn.it

[3]Department of Physics and Astronomy, Texas A&M University–Commerce, Commerce, Texas 75429, USA

[4]Dipartimento di Fisica e Astronomia "E. Majorana," Università degli Studi di Catania, 95131 Catania, Italy

[5]Centro Siciliano di Fisica Nucleare e Struttura della Materia (CSFNSM), 95123 Catania, Italy

[6]Fachbereich Physik, Institut für Kernphysik, Technische Universität Darmstadt, 64289 Darmstadt, Germany

[7]GSI Helmholtzzentrum für Schwerionenforschung GmbH, 64291 Darmstadt, Germany

Annu. Rev. Nucl. Part. Sci. 2021. 71:345–76

First published as a Review in Advance on June 25, 2021

The *Annual Review of Nuclear and Particle Science* is online at nucl.annualreviews.org

https://doi.org/10.1146/annurev-nucl-102419-033642

Keywords

nuclear astrophysics, indirect methods, direct reactions, nucleosynthesis

Abstract

The Trojan Horse Method (THM) represents an indirect path to determine the bare nucleus astrophysical *S*-factor for reactions among charged particles at astrophysical energies. This is achieved by measuring the quasi-free cross section of a suitable three-body process. The method is also suited to study neutron-induced reactions, especially in the case of radioactive ion beams. A comprehensive review of the theoretical as well as experimental features behind the THM is presented here. An overview is given of some recent applications to demonstrate the method's practical use for reactions that have a great impact on selected astrophysical scenarios.

Contents

1. INTRODUCTION

All nuclei have a positive charge, and because of the Coulomb repulsion between like charges, any fusion process requires considerable energy to take place. This critical issue in nuclear astrophysics makes the study of all nucleosynthesis processes at the relevant temperatures extremely challenging. The Coulomb repulsion is indeed responsible for the exponential decrease of the cross section $\sigma(E)$ at energies that correspond to those temperatures. For this reason, the behavior of $\sigma(E)$ at low energy is usually extrapolated from higher energies (typically $E > 100$ keV) by means of the astrophysical S-factor,

$$S(E) = E\sigma(E)\exp(2\pi\eta), \quad 1.$$

where η is the Sommerfeld parameter of the colliding nuclei, and $\exp(2\pi\eta)$ is the inverse of the Gamow factor that removes the energy dependence of $\sigma(E)$ due to the barrier tunneling. However, even an easier extrapolation can be a source of additional uncertainties for $\sigma(E)$ due, for instance, to the presence of unexpected resonances.

Another critical issue in the laboratory measurement of nucleosynthesis processes is the electron screening effect. Both the target and the projectile are usually embedded in neutral/ionized atoms or molecules and lattices, and their electron clouds are responsible for a reduction of the Coulomb barrier, which leads in turn to an increased cross section for screened nuclei, $\sigma_s(E)$, compared with the cross section for bare nuclei, $\sigma_b(E)$ (1, 2). Therefore, the so-called screening factor, defined as

$$f_{\rm lab}(E) = \sigma_s(E)/\sigma_b(E) \approx \exp(\pi\eta U_e/E), \quad 2.$$

where U_e is the so-called electron screening potential (1, 2), has to be taken into account to determine the bare nucleus cross section. In the stellar plasma, the cross section $\sigma_{\rm pl}(E)$ is related to the bare nucleus cross section by a similar enhancement factor:

$$f_{\rm pl}(E) = \sigma_{\rm pl}(E)/\sigma_b(E) \approx \exp(\pi\eta U_{\rm pl}/E), \quad 3.$$

which can be calculated once the plasma screening potential U_{pl} is known, depending on important properties of the plasma such as the Debye-Hückel radius. A measurement of U_e, which is needed to calculate $\sigma_s(E)$ from Equation 2, would also improve our understanding of U_{pl}. Low-energy fusion reactions involving charged particles measured to date have indeed shown the exponential enhancement according to Equation 2 (see also Reference 2). However, the deduced U_e values are often larger than the adiabatic limit, which is provided by the atomic models as the difference between the electron binding energies of the separate atoms in the entrance channel and that of the composite atom (2, 3). This disagreement in laboratory experiments is yet to be justified, and it prevents a full understanding of the effects under astrophysical conditions.

A weak point in the laboratory approach—and thus in the deduced U_e value—is the need to make an assumption regarding the energy dependence of $\sigma_b(E)$ at ultralow energies. Thus, indirect techniques (see 4–6 and references therein) have been introduced to overcome all these difficulties, most of which involve the need to extrapolate the cross sections into the unknown. They make use of direct reaction mechanisms, such as transfer processes (stripping and pickup) and quasi-free (QF) reactions (knockout reactions). In particular, the Trojan Horse Method (THM) (for recent reviews, see 6–10) provides a successful alternative path to determine $\sigma_b(E)$ for reactions between charged particles. It has been successfully applied many times in the last two decades to reactions connected with fundamental astrophysical problems (see 11–13 and references therein). In the last few years, reactions involving heavier systems, such as ^{12}C, have been investigated (14). Here we review the basic ideas of the THM and show some recent results. We start with a comprehensive theoretical overview from the original idea to the most updated developments. Then we describe applications of the method to determine the reaction rates relevant for astrophysics.

2. GENERAL FEATURES OF THE TROJAN HORSE METHOD

The original idea to use breakup reactions as an indirect method to investigate low-energy charged particle reactions relevant for nuclear astrophysics was introduced in References 15 and 16. In this approach, the binary rearrangement reaction to be determined at sub-Coulomb energies,

$$A + x \rightarrow C + c, \qquad 4.$$

is replaced by a suitable high-energy reaction with a three-body final state,

$$A + a \rightarrow C + c + s, \qquad 5.$$

which is called a Trojan Horse (TH) reaction. Particle a, the TH, is assumed to be a well-clustered nucleus with a $x \oplus s$ cluster configuration as the major component of its wave function. The TH reaction can be seen as a transfer to the continuum, where the TH nucleus a breaks up into x, the transferred nucleus, and s, the spectator to the subprocess. The link between the cross sections of the two reactions is established with the help of the theory of direct reactions. Since the cluster x is bound in the TH nucleus a and moves with a certain distribution of momenta, the so-called Fermi motion, it is possible that low energies in the $A + x$ relative motion can be reached despite the large energy in the $A + a$ relative motion. At the same time, the electron screening will be negligible. The TH reaction is supposed to be surface dominated, and the usual reduction of the cross section of the subprocess by the Coulomb barrier will be suppressed because the particle x is brought close to the nucleus A inside the TH particle a at high energy. In this original proposal of the THM, the tail of the $x + s$ wave function in momentum space is explored. This interpretation, however, was later superseded. It was realized that the TH reaction has to be studied under QF conditions for a successful application of the THM in experiments. These kinematic conditions correspond to the region close to the maximum of the $x + s$ momentum

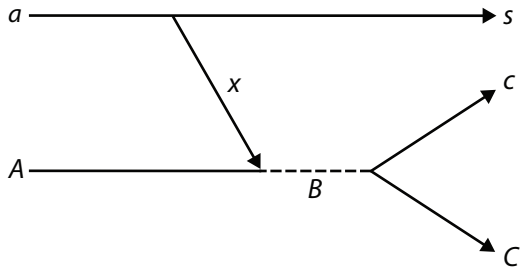

Figure 1

Scheme of a quasi-free Trojan Horse reaction. The upper vertex shows the $a \rightarrow x + s$ breakup. The lower vertex shows the reaction of astrophysical interest, which proceeds through the formation of intermediate system B.

distribution where the momentum transfer to the spectator s is small. In this selected part of the three-body phase space, the QF process gives the main contribution to the cross section of the TH reaction compared with other mechanisms (e.g., sequential or compound-nucleus reactions). The QF reaction mechanism can be represented using a pole diagram (17) (see **Figure 1**) with two vertices, one referring to the breakup of a (upper vertex in **Figure 1**) and the other to the binary reaction of astrophysical interest (lower vertex in **Figure 1**), with s as a spectator. This picture will be reflected in the expression relating the cross sections of the two reactions as a result of the theoretical description in certain approximations.

It is worth considering the kinematic conditions in more detail. Energy conservation of the TH reaction can be formulated as

$$E_{Aa} = E_{Cc} + E_{Bs} - Q_{A+a\rightarrow C+c+s} \qquad 6.$$

with the Q value

$$Q_{A+a\rightarrow C+c+s} = m_A + m_a - m_C - m_c - m_s \qquad 7.$$

and the kinetic energies of relative motion $E_{ij} = p_{ij}^2/(2\mu_{ij})$ of two particles i and j that depend on the relative momenta $\vec{p}_{ij} = \mu_{ij}(\vec{p}_i/m_i - \vec{p}_j/m_j)$ and reduced masses $\mu_{ij} = m_i m_j/(m_i + m_j)$. The combined system $C + c$ with total momentum $\vec{p}_B = \vec{p}_C + \vec{p}_c$ and mass $m_B = m_C + m_c$ is denoted below as B. Introducing the binding energy $B_{xs} = m_x + m_s - m_a > 0$ of the TH particle a and using energy conservation of the two-body reaction, the effective kinetic energy

$$E_{Ax} = E_{Cc} + m_C + m_c - m_A - m_x = E_{Aa} - E_{Bs} - B_{xs} \qquad 8.$$

in the initial state of the subprocess is expressed by means of the energies of the TH reaction. Momentum conservation of this reaction,

$$\vec{p}_A + \vec{p}_a = \vec{p}_C + \vec{p}_c + \vec{p}_s = \vec{p}_B + \vec{p}_s, \qquad 9.$$

provides a further constraint for the kinematics.

The QF condition of zero momentum transfer to the spectator s determines its momentum as $\vec{p}_s = m_s\vec{p}_a/m_a$—that is, no change in velocity. In the center-of-mass system of the TH reaction, the relative momenta are given by $\vec{p}_{Aa} = \vec{p}_A = -\vec{p}_a$ and $\vec{p}_{Bs} = \vec{p}_B = -\vec{p}_s$, and thus

$$E_{Bs} = \frac{p_s^2}{2\mu_{Bs}} = \left(\frac{m_s}{m_a}\right)^2 \frac{p_a^2}{2\mu_{Bs}} = \left(\frac{m_s}{m_a}\right)^2 \frac{\mu_{Aa}}{\mu_{Bs}} E_{Aa}. \qquad 10.$$

It follows that the QF energy

$$E_{Ax}^{\mathrm{QF}} = \left[1 - \left(\frac{m_s}{m_a}\right)^2 \frac{\mu_{Aa}}{\mu_{Bs}}\right] E_{Aa} - B_{xs} \qquad 11.$$

in the entrance channel of the two-body reaction is completely determined by the energy in the initial state of the TH reaction. It can become very small and even negative depending on the binding energy B_{xs} of the TH particle a and the choice of E_{Aa} since the prefactor of E_{Aa} is smaller than one. However, a change of E_{Ax}^{QF} is not accomplished in real experiments by changing E_{Aa}. It is usually more suitable to keep the beam energy at a fixed value and to explore a certain range in p_s and thus p_{xs} around its QF value $p_{xs}^{\mathrm{QF}} = 0$ with an upper limit $\kappa_{xs} = \sqrt{2\mu_{xs}B_{xs}}$ that represents the on-energy-shell (OES) wave number of the bound state of a. This procedure, outlined first in Reference 18, is indeed a different approach to the THM compared with the original idea from Reference 15, where the relevant values of p_{xs} were much larger (of the order of hundreds of MeV/c) because a high p_{xs} was needed to compensate for the energy of the $A + a$ relative motion. The amplitude of the momentum distribution at such high momenta can be very small compared with that at $p_{xs} = 0$, and it becomes critical to separate the QF process from other competitive reaction mechanisms. Since the analysis of the experimental data relies on the shape of the momentum distribution, a reliable theoretical description is required. This is more challenging for the tail than at small p_{xs} values. The finite range of p_{xs} in the intercluster motion is needed only to select the region of astrophysical energies that is accessible in the TH experiment. Usually it is of the order of few tens of MeV/c. A typical momentum distribution analysis is shown in **Figure 2** for the $^{18}\mathrm{O}(p, \alpha)^{15}\mathrm{N}$ reaction studied using $^{2}\mathrm{H}$ as the TH nucleus (19). **Figure 2** shows

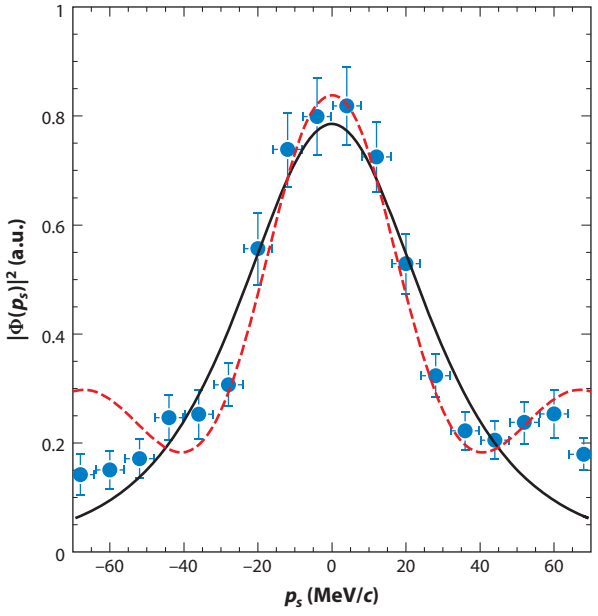

Figure 2

Experimental momentum distribution for the spectator (*blue circles*) from Reference 19 compared with theoretical ones, given in plane-wave impulse approximation (*solid black line*) and distorted-wave Born approximation (*dashed red line*) normalized to the experimental maximum. Figure adapted with permission from Reference 19; copyright 2010 The American Astronomical Society.

the experimental momentum distribution compared with the theoretical ones, given in plane-wave impulse approximation (PWIA) by the square of the Hulthén wave function in momentum space and calculated in the framework of the distorted-wave Born approximation (DWBA) using the FRESCO code (20) with optical potential parameters extrapolated from Reference 21. The two curves are scaled to the experimental maximum for comparison. Agreement is apparent within experimental errors for a neutron momentum $p_s \leq 50$ MeV/c (matching the $\kappa_{xs} = \sqrt{2\mu_{xs}B_{xs}}$ value for deuterons), and this regulates the selection of QF events for further data analysis.

If the momentum of particle x in the subprocess of the TH reaction were calculated as $\vec{p}_x = \vec{p}_a - \vec{p}_s = (1 - m_s/m_a)\vec{p}_a$ using the QF condition, the momentum

$$\vec{p}_{Ax} = \mu_{Ax}\left(\frac{\vec{p}_A}{m_A} - \frac{\vec{p}_x}{m_x}\right) = -\mu_{Ax}\left[\frac{1}{m_A} + \left(1 - \frac{m_s}{m_a}\right)\frac{1}{m_x}\right]\vec{p}_a \qquad 12.$$

would enter in the usual dispersion relation of the relative energy

$$E_{Ax} = \frac{p_{Ax}^2}{2\mu_{Ax}} = \mu_{Ax}\mu_{Aa}\left[\frac{1}{m_A} + \left(1 - \frac{m_s}{m_a}\right)\frac{1}{m_x}\right]^2 E_{Aa}, \qquad 13.$$

which is clearly different from E_{Ax}^{QF}. Hence, the subprocess in the TH reaction is off the energy shell, and x has to be considered as a virtual particle.

The QF condition that p_{xs} should be close to zero also affects the choice of TH nuclei used in actual TH experiments. A dominance of the QF reaction mechanism is expected at the maximum of the momentum distribution. Hence, TH nuclei with a strong cluster component in an S-wave of relative motion are preferred—for instance, ^{2}H for two-body reactions with protons or neutrons or ^{6}Li for the transfer of deuterons or α particles.

3. THEORY OF THE TROJAN HORSE METHOD

The theoretical description of the TH reaction can follow different approaches to establish the relation of the TH cross section to that of the binary reaction of astrophysical interest. It can be split into two separate steps: a first one that expresses the cross sections in terms of kinematic quantities and the corresponding transition matrix elements, and a second one to actually calculate the matrix elements. Different approximations that have been used in the literature for the latter step are discussed below.

3.1. Cross Sections

There is a standard way to derive expressions for the cross sections of reactions with two and three particles in the final state (see, e.g., 22, 23). These expressions depend on the choice of a reference frame and the selection of the measured quantities in the final state. For the binary reaction, the final state is described by two momenta (i.e., six variables). Energy and momentum conservation reduces the number to two independent quantities—for instance, the emission angles $\Omega_{Cc} = (\theta_{Cc}, \phi_{Cc})$ of the relative motion of the ejecta. Then the differential cross section assumes the form

$$\frac{\mathrm{d}\sigma_{A+x\to C+c}}{\mathrm{d}\Omega_{Cc}} = \frac{\mu_{Ax}\mu_{Cc}}{(2\pi)^2\hbar^4}\frac{p_{Cc}}{p_{Ax}}\frac{1}{(2J_A+1)(2J_x+1)}\sum_{M_AM_x}\sum_{M_CM_c}|T_{A+x\to C+c}|^2 \qquad 14.$$

with the usual summation over spin projections, M_C and M_c, in the final state and averaging over that in the initial state, M_A and M_x, for nuclei with total angular momenta J_A and J_x, respectively. Corresponding expressions to Equation 14 can be given for the TH reaction. Here the final state

is fully characterized by $(3 \times 3) - 4 = 5$ independent variables, and it is possible to choose different combinations of quantities that are observed in the final state. Choosing the energy and momentum direction of a particle i and the momentum direction of a particle j as kinematic quantities, the differential cross section is given by

$$\frac{\mathrm{d}\sigma_{A+a\to C+c+s}}{\mathrm{d}E_i \mathrm{d}\Omega_i \mathrm{d}\Omega_j} = \frac{\mu_{Aa} m_i m_j}{(2\pi)^5 \hbar^7} \frac{p_i p_j}{p_{Aa}} \left[1 + \frac{m_j}{m_k}\left(1 - \frac{\vec{P}_{(jk)} \cdot \vec{p}_j}{p_j^2}\right)\right]^{-1} \frac{1}{(2J_A+1)(2J_a+1)} \sum_{M_A M_a} \sum_{M_C M_c M_s} |T_{A+a\to C+c+s}|^2 , \quad 15.$$

where $\vec{P}_{(jk)} = \vec{p}_A + \vec{p}_a - \vec{p}_i$, and the particle k is not detected in the experiment. Alternatively, relative coordinates can be used for the following result:

$$\frac{\mathrm{d}\sigma_{A+a\to C+c+s}}{\mathrm{d}E_{ij} \mathrm{d}\Omega_{ij} \mathrm{d}\Omega_{(ij)k}} = \frac{\mu_{Aa} \mu_{ij} \mu_{(ij)k}}{(2\pi)^5 \hbar^7} \frac{p_{ij} p_{(ij)k}}{p_{Aa}} \frac{1}{(2J_A+1)(2J_a+1)} \sum_{M_A M_a} \sum_{M_C M_c M_s} |T_{A+a\to C+c+s}|^2 , \quad 16.$$

which has a simpler structure than Equation 15. The T-matrix elements $T_{A+x\to C+c}$ and $T_{A+a\to C+c+s}$ in Equations 14–16 contain the essential information on the reaction and are considered in the following section.

3.2. Transition Matrix Elements

The T-matrix element of the TH reaction has been considered in different approximations in the literature. The simplest approach is the PWIA (see, e.g., 24), which was originally used for reactions at high energies. It provides a simple expression for the cross sections in factorized form. However, a heuristic modification was necessary to account for the effect of the reduced Coulomb barrier penetration. Other approaches use the plane-wave Born approximation (PWBA) or the DWBA to derive the relation of the cross sections for the TH reaction and the two-body subprocess. They provide an explanation for the Coulomb penetration correction in the modified PWIA. To simplify the notation, spins of the particles are not considered below, and relative coordinates are used. General expressions with full angular momentum coupling can be found in the original literature. Antisymmetrization is also not taken into account.

3.2.1. Modified plane-wave impulse approximation. The PWIA is the simplest approach to understand the main features of the TH theory. The T-matrix elements of the two reactions of interest can be written in symbolic form as

$$T_{A+x\to C+c}(\vec{p}_{Cc}, \vec{p}_{Ax}) = \langle \psi_{Cc}(\vec{p}_{Cc}) | \hat{T}_{A+x\to C+c} | \psi_{Ax}(\vec{p}_{Ax}) \rangle \quad 17.$$

and

$$T_{A+a\to C+c+s}(\vec{p}_{Cc}, \vec{p}_{Bs}, \vec{p}_{Aa}) = \langle \psi_{Ccs}(\vec{p}_{Cc}, \vec{p}_{Bs}) | \hat{T}_{A+a\to C+c+s} | \psi_{Aa}(\vec{p}_{Aa}) \rangle \quad 18.$$

with the corresponding transition operators $\hat{T}_{A+x\to C+c}$ and $\hat{T}_{A+a\to C+c+s}$, which are solutions to the appropriate integral equations for reactions in general (22). The wave functions $\psi_{ij}(\vec{p}_{ij}) = \phi_i \phi_j \exp(i\vec{p}_{ij} \cdot \vec{r}_{ij}/\hbar)$ and $\psi_{ijk}(\vec{p}_{ij}, \vec{p}_{(ij)k}) = \phi_i \phi_j \phi_k \exp[i(\vec{p}_{ij} \cdot \vec{r}_{ij} + \vec{p}_{(ij)k} \cdot \vec{r}_{(ij)k})/\hbar]$ in Equations 17 and 18 are given by plane waves for the relative motion of the nuclei i, j, and k

with internal cluster wave functions denoted by ϕ_A, ϕ_a, ϕ_C, ϕ_c, ϕ_s, and ϕ_x. The ground state wave function of the TH can be written in the cluster approximation as

$$\phi_a = \phi_x \phi_s \chi_{xs}(\vec{r}_{xs}) = \phi_x \phi_s \int \frac{\mathrm{d}^3 q}{(2\pi\hbar)^3}\, \tilde{\chi}_{xs}(\vec{q})\, \exp(i\vec{q}\cdot\vec{r}_{xs}/\hbar) \qquad 19.$$

with the wave function of relative motion $\chi_{xs}(\vec{r}_{xs})$ in coordinate space and $\tilde{\chi}_{xs}(\vec{q})$ in momentum space. The essential step in the PWIA is to replace $\hat{T}_{A+a\to C+c+s}$ in Equation 18 with $\hat{T}_{A+x\to C+c}$, assuming that the spectator s is not involved in the TH reaction. A change of coordinates from $\vec{r}_{Aa}$ and $\vec{r}_{xs}$ to $\vec{r}_{Bb}$ and $\vec{r}_{Ax}$ and integration over $\vec{r}_{Bs}$ and $\vec{q}$ (see 25) lead to the factorization

$$T^{\mathrm{PWIA}}_{A+a\to C+c+s}(\vec{p}_{Cc}, \vec{p}_{Bs}, \vec{Q}_{Aa}) = \tilde{\chi}_{xs}(\vec{Q}_{Bs})\, T_{A+x\to C+c}(\vec{p}_{Cc}, \vec{Q}_{Aa}) \qquad 20.$$

with the momenta $\vec{Q}_{Aa} = \vec{p}_{Aa} - \frac{m_A}{m_A+m_x}\vec{p}_{Bb}$ and $\vec{Q}_{Bs} = \vec{p}_{Bs} - \frac{m_s}{m_x+m_s}\vec{p}_{Aa}$. The meaning of the argument $\vec{Q}_{Bs}$ of the momentum space wave function $\tilde{\chi}_{xs}$ is most easily seen in the center-of-mass system. In this case, $\vec{Q}_{Bs} = \frac{m_s}{m_x+m_s}\vec{p}_a - \vec{p}_s$; that is, it is the (negative) momentum transfer to the spectator s, and thus the QF scattering condition corresponds to $\vec{Q}_{Bs} = 0$. Combining Equation 20 with the expressions of the cross sections from Equations 14 and 16, the relation

$$\frac{\mathrm{d}\sigma_{A+a\to C+c+s}}{\mathrm{d}E_{Cc}\mathrm{d}\Omega_{Cc}\mathrm{d}\Omega_{Bs}} = K \left|\tilde{\chi}_{xs}(\vec{Q}_{Bs})\right|^2 \frac{\mathrm{d}\sigma^{\mathrm{HOES}}_{A+x\to C+c}}{\mathrm{d}\Omega_{Cc}} \qquad 21.$$

is obtained with a kinematic factor

$$K = \frac{\mu_{Aa}\mu_{Bs}}{(2\pi\hbar)^3\mu_{Ax}} \frac{p_{Ax}p_{Bs}}{p_{Aa}} \frac{2J_x+1}{2J_a+1} \qquad 22.$$

if the choice of $i = C, j = c$, and $k = s$ is made and relative coordinates are used to specify the final state. Similar relations are found for other choices of the kinematic variables. The cross section of the two-body reaction in Equation 21 carries the superscript HOES (half off the energy shell) because the momentum in the entrance channel of the two-body reaction is not $\vec{p}_{Ax}$, as required by energy conservation, but $\vec{Q}_{Aa}$.

Equation 21 shows the typical structure with three factors as a result of the PWIA: a kinematic factor, a momentum distribution, and a cross section of the two-body subprocess. In this form, however, it is not directly applicable in the THM. The HOES cross section has to be converted to the OES cross section from Equation 14 for the reaction of interest. This is accomplished heuristically by introducing a simple factor,

$$\frac{\mathrm{d}\sigma^{\mathrm{HOES}}_{A+x\to C+c}}{\mathrm{d}\Omega_{Cc}} = \frac{\mathrm{N}}{T_{Ax}} \frac{\mathrm{d}\sigma_{A+x\to C+c}}{\mathrm{d}\Omega_{Cc}}, \qquad 23.$$

with a normalization constant N and penetrability T_{Ax}. The latter is assumed to compensate for the Coulomb suppression of the cross section in the regular OES two-body reaction. The Coulomb penetrability is defined in general as

$$T_{Ax} = \left[F^2_{l_{Ax}}(k_{Ax}R_{Ax}) + G^2_{l_{Ax}}(k_{Ax}R_{Ax})\right]^{-1} \qquad 24.$$

with regular and irregular Coulomb wave functions F_l and G_l, respectively. It depends on the orbital angular momentum l_{Ax} and momentum $\hbar k_{Ax} = p_{Ax}$ and is calculated at a certain radius R_{Ax}. For $l_{Ax} = 0$, which is valid for almost all applications of the THM, the limit $R_{Ax} \to 0$ can be taken for the following result:

$$T_{Ax} \to \frac{2\pi\eta_{Ax}}{\exp(2\pi\eta_{Ax}) - 1}, \qquad 25.$$

where the Sommerfeld parameter,

$$\eta_{Ax} = \frac{Z_A Z_x e^2}{\hbar} \frac{\mu_{Ax}}{p_{Ax}}, \qquad 26.$$

contains the charge numbers Z_A and Z_x of the nuclei in the entrance channel of the two-body reaction. At low energies E_{Ax}, η_{Ax} becomes very large, and the factor p_{Ax} in the kinematic factor (Equation 22) combines with the penetrability as

$$\frac{p_{Ax}}{T_{Ax}} \to \frac{p_{Ax}}{2\pi\eta_{Ax}} \exp(2\pi\eta_{Ax}) \propto E_{Ax} \exp(2\pi\eta_{Ax}), \qquad 27.$$

which is the factor in the usual definition (Equation 1) of the astrophysical S-factor. It shows only a weak energy dependence in the absence of resonances and is used frequently for the extrapolation of cross sections to low energies. Hence, the THM gives direct access to the S-factor of low-energy reactions of astrophysical interest. The introduction of the factor N/T_{Ax} in Equation 23 needs a justification that is found with improved approximations of the T-matrix element in Equation 16. Nevertheless, it is the standard description used in most experimental applications of the THM.

3.2.2. Postform distorted-wave and plane-wave Born approximations. This approach was developed in References 25 and 26 to justify the heuristic penetrability correction (Equation 23) to relate the HOES and OES cross sections for the two-body subprocess. It was used in the first successful applications of the THM (18, 27–32). For a transfer reaction to a bound state in the final $B = C + c$ system (i.e., $A + a \to B + s$), the exact T-matrix element is given by the postform expression

$$T^{\text{post}}_{A+a\to B+s} = \langle \phi_B \phi_s \chi^{(-)}_{Bs}(\vec{p}_{Bs}) | V_{Bs} - U_{Bs} | \Psi^{(+)}_{Aa}(\vec{p}_{Aa}) \rangle \qquad 28.$$

with the full many-body interaction V_{Bs} in the final state, a distorted wave $\chi^{(-)}_{Bs}$ generated from the optical potential U_{Bs}, and the full solution of the scattering problem $\Psi^{(+)}_{Aa}$ in the initial state. In the application to the THM, a transfer reaction to the continuum, the bound state wave function ϕ_B is replaced by the scattering wave function $\Psi^{(-)}_{Cc}(\vec{p}_{Cc})$, and the full solution $\Psi^{(+)}_{Aa}$ is approximated by a distorted wave $\phi_A \phi_a \chi^{(+)}_{Aa}(\vec{p}_{Aa})$. Then one arrives at the following postform DWBA:

$$T^{\text{DWBA,post}}_{A+a\to C+c+s} = \langle \Psi^{(-)}_{Cc}(\vec{p}_{Cc}) \phi_s \chi^{(-)}_{Bs}(\vec{p}_{Bs}) | V_{Bs} - U_{Bs} | \phi_A \phi_a \chi^{(+)}_{Aa}(\vec{p}_{Aa}) \rangle, \qquad 29.$$

where the imaginary parts of the optical potentials cause a strong suppression of the wave function amplitudes at small distances of the clusters. Hence, the main contribution arises from the external part of the many-body integral, and the internal part can be neglected. It is customary in the theory of direct reactions to replace the full transition potential $V_{Bs} - U_{Bs}$ by the approximation V_{xs}. Then, similar to Equation 19, it is possible to introduce a momentum amplitude W through the relation

$$V_{xs}\phi_a = \phi_x \phi_s \int \frac{\mathrm{d}^3 q}{(2\pi\hbar)^3} W(\vec{q}) \exp(i\vec{q} \cdot \vec{r}_{xs}/\hbar), \qquad 30.$$

which can be expressed as $W(\vec{q}) = -[B_{xs} + q^2/(2\mu_{xs})]\tilde{\chi}_{xs}(\vec{q})$ when the Schrödinger equation for the bound state wave function ϕ_a is used.

The two-body subprocess can be considered a peripheral reaction at the low energies of interest. Thus, the full scattering wave function can be replaced by its asymptotic form for large distances r_α of the clusters in all channels $\alpha = Cc, Ax, \ldots$. It is given by

$$\Psi^{(\pm)}_{Cc}(\vec{p}_{Cc}) \to \frac{4\pi}{k_{Cc}} \sum_\alpha \sum_{lm} \frac{\xi^{(\pm)}_l(\alpha, r_\alpha)}{r_\alpha} i^l Y_{lm}(\hat{r}_\alpha) Y^*_{lm}(\hat{k}_{Cc}) \, \Phi_\alpha \qquad 31.$$

when an expansion in partial waves is introduced with $\vec{p}_{Cc} = \hbar k_{Cc}$. The Φ_α describes the internal wave functions of the clusters (e.g., $\Phi_{Cc} = \phi_C \phi_c$, $\Phi_{Ax} = \phi_A \phi_x$). The radial wave function in a channel α

$$\xi_l^{(+)}(\alpha, r_\alpha) = \frac{1}{2i}\sqrt{\frac{v_{Cc}}{v_\alpha}}\left[S^l_{\alpha Cc} u_l^{(+)}(k_\alpha, r_\alpha) - \delta_{\alpha Cc} u_l^{(-)}(k_\alpha, r_\alpha)\right] \qquad 32.$$

with $\xi_l^{(-)}(\alpha) = \xi_l^{(+)*}(\alpha)$ contains the channel velocities $v_\alpha = p_\alpha/\mu_\alpha$, the S-matrix elements $S^l_{\alpha Cc}$ for the reaction $C + c \to \alpha$, and linear combinations $u_l^{(\pm)}(k_\alpha, r_\alpha) = \exp[\mp i\sigma_l(\eta_\alpha)]\,[G_l(k_\alpha r_\alpha) \pm iF_l(k_\alpha r_\alpha)]$ of the Coulomb wave functions with Coulomb phase shifts σ_l. With the selection of the channel $\alpha = Ax$, the results above combine to the approximation

$$T^{\mathrm{DWBA,post}}_{A+a\to C+c+s} = \frac{1}{2ik_{Cc}}\sqrt{\frac{v_{Cc}}{v_{Ax}}}\sum_l (2l+1) \qquad 33.$$
$$\left[S^l_{AxCc}\, U_l^{(+)}(\vec{p}_{Bs}, \vec{p}_{Cc}, \vec{p}_{Aa}) - \delta_{AxCc} U_l^{(-)}(\vec{p}_{Bs}, \vec{p}_{Cc}, \vec{p}_{Aa})\right]$$

of the T-matrix element with functions $U_l^{\pm}(\vec{p}_{Bs}, \vec{p}_{Cc}, \vec{p}_{Aa})$, which are defined in Reference 26. This result closely resembles the definition of the scattering amplitude

$$f(Cc \to Ax) = \frac{4\pi}{2ik_{Cc}}\sqrt{\frac{v_{Cc}}{v_{Ax}}}\sum_{lm} Y^*_{lm}(\hat{r}_{Ax}) Y_{lm}(\hat{k}_{Cc})\left[S^l_{AxCc} - \delta_{AxCc}\right], \qquad 34.$$

which appears in the cross section

$$\frac{\mathrm{d}\sigma}{\mathrm{d}\Omega_{Ax}}(Cc \to Ax) = \frac{v_{Ax}}{v_{Cc}}\left|f(Cc \to Ax)\right|^2 \qquad 35.$$

of the reaction $C + c \to A + x$. Since it is the inverse of the subprocess of interest, its cross section is easily transformed to that of the inverse reaction with the help of the theorem of detailed balance. The calculation of the functions $U_l^{(\pm)}$ is rather complicated in general, and there is no simple connection between the T-matrix element (Equation 33) and the scattering amplitude (Equation 34) if many partial waves contribute. In particular, the momentum distribution W does not appear as an overall factor.

A connection to the PWIA can be made when the distorted waves $\chi^{(+)}_{Aa}$ and $\chi^{(-)}_{Bs}$ in Equation 29 are replaced by plane waves. Following the same steps as in the derivation of Equation 20, the result

$$T^{\mathrm{PWBA,post}}_{A+a\to C+c+s} = W(\vec{Q}_{Bs})\,\langle \Psi^{(-)}_{Cc}(\vec{p}_{Cc})|\phi_A\phi_x \exp(i\vec{Q}_{Aa}\cdot\vec{r}_{Ax})\rangle \qquad 36.$$

in the postform PWBA is obtained with a factorization as in the PWIA. Introducing the partial-wave expansion of $\Psi^{(-)}_{Cc}$, the T-matrix element (Equation 36) assumes a product form

$$T^{\mathrm{PWBA,post}}_{A+a\to C+c+s} = \frac{\hbar}{k_{Ax}Q_{Aa}}\, W(\vec{Q}_{Bs})\, f_{\mathrm{THM}}(Cc \to Ax) \qquad 37.$$

with the THM scattering amplitude

$$f_{\mathrm{THM}}(Cc \to Ax) = \frac{4\pi}{2ik_{Cc}}\sqrt{\frac{v_{Cc}}{v_{Ax}}}\sum_{lm} Y^*_{lm}(\hat{Q}_{Aa}) Y_{lm}(\hat{k}_{Cc}) \qquad 38.$$
$$\left[S^l_{AxCc} J_l^{(+)}(R, k_{Ax}, Q_{Aa}) - \delta_{AxCc} J_l^{(-)}(R, k_{Ax}, Q_{Aa})\right],$$

which includes the off-shell effects explicitly in the form of dimensionless functions $J_l^{(\pm)}$, which are defined and studied in detail in Reference 26. The scattering angle is defined with respect to

the direction of $\vec{Q}_{Aa}$ instead of $\vec{r}_{Ax}$. Finally, if only one partial wave l contributes to the reaction, the relation

$$\frac{\mathrm{d}\sigma_{A+a\to C+c+s}}{\mathrm{d}E_{Cc}\mathrm{d}\Omega_{Cc}\mathrm{d}\Omega_{Bs}} = \frac{\mu_{Aa}\mu_{Bs}}{(2\pi\hbar)^3\mu_{Ax}}\frac{p_{Ax}p_{Bs}}{p_{Aa}}\frac{2J_x+1}{2J_a+1}\left|\tilde{\chi}_{xs}(\vec{Q}_{Bs})\right|^2 F_l \frac{\mathrm{d}\sigma_l}{\mathrm{d}\Omega_{Aa}}(Ax\to Cc) \qquad 39.$$

of the cross sections with the dimensionless factor

$$F_l = \frac{1}{(2\pi)^2 v_{Ax}^2 Q_{Aa}^2}\left(B_{xs}+\frac{Q_{Bs}^2}{2\mu_{xs}}\right)^2\left|J_l^{(+)}\right|^2 \qquad 40.$$

is found and can be compared immediately with Equations 21–23. As shown in Reference 26, the integrals $J_l^{(\pm)}$ behave as $(k_{Ax}/Q_{Aa})^{3/2}\exp(\pi\eta_{Ax})$ for low energies E_{Ax}, and thus $F_l \propto k_{Ax}\exp(2\pi\eta_{Ax})$, which is the inverse of the penetrability T_{Ax} in Equation 25. Hence, the conversion of the HOES cross section to the OES cross section in Equation 23 is well founded.

The calculation of the functions $J_l^{(\pm)}$, and more generally that of the functions $U_l^{(\pm)}$ in Equation 33, is a delicate numeric problem because it involves a product of radial scattering wave functions in the integrals with an infinite upper boundary. The origin of this difficulty can be traced back to the replacement of a bound state wave function ϕ_B in the T-matrix element (Equation 28) by a scattering wave function $\Psi_{Cc}^{(-)}$. In contrast, for a transfer reaction to a bound state, the integrals converge properly because of the exponential decrease of the radial wave functions. The numeric problem can be circumvented in a different approach, which is described in the following subsection.

3.2.3. Prior-form distorted-wave Born approximation and surface-integral approach. Instead of using the postform expression (Equation 29) for the T-matrix element of the THM reaction, it is possible to start with the exact prior-form expression

$$T_{A+a\to B+s}^{\mathrm{prior}} = \langle\Psi_{Ccs}^{(-)}(\vec{p}_{Cc},\vec{p}_{Bs})|V_{Aa}-U_{Aa}|\phi_A\phi_a\chi_{Aa}^{(+)}(\vec{p}_{Aa})\rangle \qquad 41.$$

in obvious notation for the wave functions and potentials. The full solution of the three-body scattering problem $\Psi_{Ccs}^{(-)}(\vec{p}_{Cc},\vec{p}_{Bs})$ is replaced in the DWBA by $\Psi_{Cc}^{(-)}(\vec{p}_{Cc})\phi_s\chi_{Bs}^{(-)}(\vec{p}_{Bs})$ as in Section 3.2.2. This expression has been used to introduce the surface-integral approach as developed in References 33 and 34 and applied to the THM (see, e.g., the review in 35). The matrix element is split into two contributions:

$$T_{A+a\to B+s}^{\mathrm{DWBA,prior}} = T_{A+a\to B+s,\mathrm{int}}^{\mathrm{DWBA,prior}} + T_{A+a\to B+s,\mathrm{ext}}^{\mathrm{DWBA,prior}}, \qquad 42.$$

where the integration over r_{Ax} is limited to the intervals $[0, R_{Ax}]$ and $[R_{Ax}, \infty]$, respectively, with a channel radius R_{Ax}. The external matrix element is small and can be neglected with a reasonable choice of the channel radius R_{Ax}. The main point of the surface-integral approach is that the transition potential in the internal matrix element is now rewritten as

$$\begin{aligned} V_{Aa}-U_{Aa} &= V_{As}+V_{Ax}-U_{Aa} \qquad 43.\\ &= (V_{As}+V_{xs}-U_{Bs})-(V_{xs}+U_{Aa})+(V_{Ax}+U_{Bs}) \end{aligned}$$

with three operators in parentheses. The first is the transition potential $V_{Bs}-U_{Bs}$ as in the postform DWBA matrix element (Equation 29). The latter two terms can be identified with the potentials in the Schrödinger equations of the initial and final channel wave functions with Hamiltonians $H_i = m_A + m_x + m_s + T_{xs} + V_{xs} + T_{Aa} + U_{Aa}$ and $H_f = m_C + m_c + m_s + T_{Cc} + V_{Cc} + T_{Bs} +$

U_{Bs} when using $V_{Ax} = V_{Cc}$. Hence, the internal contribution can be transformed into

$$T^{\mathrm{DWBA,prior}}_{A+a\to B+s,\mathrm{int}} = T^{\mathrm{DWBA,post}}_{A+a\to B+s,\mathrm{int}} - \langle \Psi^{(-)}_{Cc}(\vec{p}_{Cc})\phi_s \chi^{(-)}_{Bs}(\vec{p}_{Bs})|\ \overleftarrow{T} - \overrightarrow{T}\ |\phi_A\phi_a\chi^{(+)}_{Aa}(\vec{p}_{Aa})\rangle \qquad 44.$$

with the kinetic energy operator of relative motions $T = T_{xs} + T_{Aa} = T_{Cc} + T_{Bs} = T_{Ax} + T_{Bs}$ acting on the bra and ket state and expressed in different sets of Jacobi coordinates. It is essential that the matrix element with the kinetic energy operators not vanish as for a Hermitian operator because the wave functions do not belong to the proper class of functions. The internal postform matrix element in Equation 44 can be neglected, as in Section 3.2.2, because it is small. It is argued in Reference 34 that the kinetic energy operator T_{Bs} gives no contribution to the second matrix element and that only the T_{Ax} part remains. Then, a final partial integration with respect to the coordinate $\vec{r}_{Ax}$ leads to a surface integral over a sphere with channel radius R_{Ax} but volume integrals with respect to the other coordinates.

This surface-integral reformulation of the T-matrix element is useful because the calculation of integrals with external wave functions over an infinite volume is avoided. It is also possible to establish a direct connection to R-matrix theory (36) (see below), introducing parameters like the reduced width amplitudes if the TH reaction proceeds through a resonance in the $A + x$ system in the intermediate state before decaying into the $C + c$ channel (35). This treatment of the TH reaction, however, raises a new question. The DWBA-type calculation of the T-matrix element assumes a direct single-step process in the TH reaction reflected by the appearance of a single transition potential in the matrix element. The TH nucleus a breaks up into a spectator s, and the particle x is transferred to the nucleus A, initiating the reaction to the $C + c$ system. This description is reflected in the factorization of the T-matrix element (e.g., in Equations 20 and 36), or in the cross section in Equation 21, and corresponds to the two vertices in **Figure 1**. However, the (off-shell) propagation of the transferred particle x after the breakup of a and before reacting with A is not explicitly considered in the formulations discussed above. Such an approach has been studied in the context of the R-matrix surface-integral approach (e.g., 35). The picture of a two-step process is also supported when a connection of the THM to the inclusive nonelastic breakup (INEB) theory is made (37, 38). Finally, we would like to recall that since the TH reaction involves genuine three-body bound and scattering states, a Faddeev-like formulation of three-body systems (39) might be required for a more precise and quantitative description. In particular, the scattering problem with three charged particles poses a challenge in the theoretical description of the wave function asymptotics. This issue has to be explored in the future and can help to assess the validity of the approximations employed thus far. In what follows, we provide the most relevant details of the R-matrix approach (usually referred to as modified R-matrix) that is routinely used in many THM studies.

3.2.4. Connection to R-matrix theory. Assuming that the system B is populated following the a breakup and the emission of the spectator nucleus s, the TH reaction amplitude describing the process is given in the prior form by (disregarding particle spins)

$$M(P, \vec{k}_{aA}) \propto \langle \chi^{(-)}(\vec{k}_{sB})\, \Phi^{(-)}_B | \Delta V_{sB} | \varphi_a \varphi_A \Psi^{(+)}_i \rangle, \qquad 45.$$

where $\Psi^{(+)}_i$ is the exact $a + A$ scattering wave function, $\Phi^{(-)}_B$ is the wave function of the system $B = c + C = x + A$, $\chi^{(-)}(\vec{k}_{sB})$ is the distorted wave of the system $s + B$, φ_i is the i-th nucleus bound state wave function, $\vec{k}_{ij}$ is the relative momentum of nuclei i and j, $P = \{\vec{k}_{sB}, \vec{k}_{cC}\}$ is the six-dimensional momentum describing the three-body system s, c, and C, and $\Delta V_{sB} = V_{sB} - U_{sB}$. Using the spectral decomposition of the $\Phi^{(-)}_B$ wave function given by equation 3.8.1 in Reference 40, we can easily establish the connection with the R-matrix approach. Indeed, the shell model–based

resonant R-matrix representation for $\Phi_{B\tau}^{(-)}$ with respect to the τ channel is very similar to the level decomposition in the internal region of the wave function in the R-matrix approach:

$$\Phi_{B\tau}^{(-)} \propto \sum_{\nu,\mu=1}^{N} \tilde{V}_{\nu\tau}(E_\tau)\,[\mathbf{D}^{-1}]_{\nu\mu}\,\Phi_\mu. \qquad 46.$$

Here N is the number of levels in the decomposition, E_τ is the relative kinetic energy of nuclei in the τ channel, and Φ_μ is the bound state wave function of system B excited to the level μ. $\mathbf{D}_{\nu\tau}$ is the same-level matrix as in the R-matrix theory (36), given by equation 4.2.20b in Reference 40, depending on the entrance and exit channels' reduced width amplitudes, energy levels, and energy shifts. Finally,

$$\tilde{V}_{\nu\tau}(E_\tau) = \langle \chi_\tau^{(-)}\,\varphi_\tau | \Delta V_\tau | \Phi_\nu \rangle \qquad 47.$$

is the resonant form factor for the ν resonance level decay described by the Φ_ν wave function into the channel τ, and $\chi_\tau^{(-)}$ is the distorted wave in the same channel. As shown, for instance, in Reference 41, such amplitude is directly connected to the formal partial resonance width for the decay of this level into the τ channel:

$$\tilde{\Gamma}_{\nu\tau}(E_\tau) = 2\pi\,|\tilde{V}_{\nu\tau}(E_\tau)|^2. \qquad 48.$$

Following the discussion in Reference 6, the amplitude (Equation 45) directly leads to the triple differential cross section of the $a + A \rightarrow c + C + s$ THM process:

$$\frac{\mathrm{d}^3\sigma}{\mathrm{d}E_{cC}\,\mathrm{d}\Omega_{\mathbf{k}_{cC}}\,\mathrm{d}\Omega_{\mathbf{k}_{sB}}} = \frac{\mu_{cC}\,\mu_{sB}\,\mu_{aA}}{2\pi^5}\,\frac{k_{cC}\,k_{sB}}{k_{aA}}\,\frac{1}{\hat{J}_a\,\hat{J}_A} \times \left| \sum_{\nu,\tau=1}^{N} \tilde{V}_{\nu\,cC}(E_{cC})\,[\mathbf{D}^{-1}]_{\nu\tau}\,M_\tau(\mathbf{k}_{sB},\mathbf{k}_{aA}) \right|^2, \qquad 49.$$

where $\hat{J} = 2J + 1$, and J_i is the spin of particle i.

Since $\mathbf{D}_{\nu\tau}$ is the same-level matrix as in the conventional R-matrix theory, the entrance and exit channels' reduced width amplitudes γ and energy levels can be extracted by fitting the experimental THM cross section and then can be used to deduce the $A(x, c)C$ astrophysical factor with no need for extrapolation down to astrophysical energies.

Equation 49 takes a simpler and more intuitive form under the assumption of isolated noninterfering resonances, explicitly showing the reduced width amplitudes γ (42–44):

$$\frac{\mathrm{d}^2\sigma}{\mathrm{d}E_{xA}\mathrm{d}\Omega_s} = \mathrm{NF} \sum_i (2J_i + 1) \times \left| \sqrt{\frac{\mathrm{k_f}(E_{xA})}{\mu_{cC}}}\,\frac{\sqrt{2P_{l_i}(k_{cC}R_{cC})}M_i(p_{xA}R_{xA})\gamma_{cC}^i\gamma_{xA}^i}{D_i(E_{xA})} \right|^2, \qquad 50.$$

where N is a normalization constant, $\mathrm{k_f}(E_{xA}) = \sqrt{2\mu_{cC}(E_{xA} + Q)}/\hbar$ (Q is the reaction Q value), P_{l_i} is the penetration factor in the l_i-wave, and R_{xA} and R_{cC} are the channel radii. Assuming that the use of plane waves is justified, a simple form for the transfer amplitude $M_i(p_{xA}R_{xA})$ can be deduced (45):

$$M_i(p_{xA}R_{xA}) = \left[(B_{xA\,i} - 1)\,j_{l_i}(\rho) - \rho\,\frac{\partial j_{l_i}(\rho)}{\partial\rho} \right]_{\rho = p_{xA}\,R_{xA}}, \qquad 51.$$

where $j_{l_i}(\rho)$ is the spherical Bessel function, $p_{xA} = \sqrt{2\mu_{xA}(E_{xA} + B_{xs})}/\hbar$ [B_{xs} is the binding energy of the $a = (x + s)$ system], and $B_{xA\,i}$ is an arbitrary boundary condition chosen, as in References 42, 44, and 46, to yield the observable resonance parameters. Finally, $D_i(E_{xA})$ is the standard R-matrix denominator in the case of one-level, two-channel R-matrix formulas (36).

4. APPLICATION OF THE TROJAN HORSE METHOD TO ASTROPHYSICAL REACTIONS

This section provides a brief overview of recent results for stable and unstable nuclei as well as highlights of the involved astrophysical scenarios. Comparison with direct data is also presented if available. In particular, we review the physics cases of ^{18}F$(p, \alpha)^{15}$O, ^{7}Be$(n, \alpha)^{4}$He, ^{19}F$(\alpha, p)^{22}$Ne, ^{3}He$(n, p)^{3}$H, and ^{12}C+^{12}C fusion.

4.1. The ^{18}F$(p, \alpha)^{15}$O Reaction in Classical Novae

Classical novae are among the most powerful explosive events in the Universe; the typical energy released in an episode is of the order of 10^{37} J (approximately the Sun's total energy output for 10^4 years). A classical nova originates in a binary system in which a white dwarf accretes material from a less evolved twin star. Owing to degenerate conditions in the accretion disk, no expansion follows compressional heating. When the temperature reaches about 7×10^7 K, degeneracy is lifted and the layers can begin to expand, yet at this stage the temperature increases so quickly that a thermonuclear runaway is triggered (47). Typical temperatures achieved in the runaway range between 10^8 and 4×10^8 K depending on white dwarf mass; in the hot, proton-rich environment of the accreted material, the hot CNO cycle is ignited, leading to proton captures and the synthesis of β^+ unstable nuclei. Recent reviews on classical novae can be found in References 47–50.

Besides representing an important energy source, radioactive nuclides with lifetimes longer than the typical expansion times determine a characteristic isotopic pattern that is very different from the one attributed to CNO equilibrium cycling. Moreover, their production indicates the opportunity to track down γ-ray emission, an additional diagnostic tool to shed light on the explosion mechanism and nucleosynthesis. Because of its half-life $T_{1/2} \sim 110$ s, ^{18}F supply would not be significantly depleted until the external layers of the nova became transparent to γ radiation (49). For this reason, it is expected that ^{18}F would provide the largest contribution to the $\leq$511-keV γ-ray emission originated by the annihilation of positrons from ^{18}F β^+ decay, which in turn is predicted to be the dominant contribution to the γ-ray spectrum.

While such considerations suggest the use of γ-ray lines from ^{18}F to constrain novae models, to date only upper limits to such lines can be set. These are converted into detectability distances, defined as the novae maximum distance for which the ^{18}F annihilation line could be detected. So far, the SPI spectrometer on the space-borne γ-ray observatory INTEGRAL has managed to establish the most accurate detectability distance of the 511-keV line, ~3 kpc (51, 52). Knowledge of the cross sections of its production and destruction paths is then a pivotal ingredient for accurate modeling of the outburst mechanism and nucleosynthesis.

4.1.1. The ^{18}F$(p, \alpha)^{15}$O reaction: status of the measurements. The main ^{18}F destruction process is the ^{18}F$(p, \alpha)^{15}$O reaction, which is ~1,000 times more efficient than the ^{18}F$(p, \gamma)^{19}$Ne reaction (50). Despite its importance, the former process is the most uncertain reaction among those affecting the ^{18}F supply, notwithstanding the theoretical and experimental studies carried out to date. The experiments can be divided into direct and indirect ones. The direct studies are challenging because the Coulomb barrier suppresses the cross section to vanishingly small values; furthermore, the need for a radioactive beam (typically of an intensity of the order of 10^6

particles per second) makes the signal-to-noise ratio extremely unfavorable. Therefore, existing studies have been unable to set stringent constraints on the trend of the astrophysical factor. Most direct measurements focus on the $3/2^+$ resonance at about 700 keV in the center-of-mass system (53–58). Few measurements have reached energies as low as 300 keV, where a $3/2^-$ resonance has been observed (59, 60).

Indirect methods, by contrast, have provided important additional constraints on the astrophysical factor. Nuclear spectroscopy of ^{19}Ne or of its ^{19}F mirror nucleus has made it possible to probe resonances at astrophysical energies. Two examples are the use of (d, p) reactions on ^{18}F and the use of ^{15}N+α elastic scattering to explore the ^{19}F excitation energies of astrophysical interest (see 61 and 62, respectively). Examples of ^{19}Ne spectroscopy include the investigation of proton inelastic scattering off ^{19}Ne (63), the (d, n) transfer reaction to ^{18}F (64), and the (p, d) neutron pickup process off ^{20}Ne (65, 66). These indirect studies suggest that low-energy S-wave resonances, and in particular the $3/2^+$ levels above and below the proton threshold at a ^{19}Ne excitation energy of about 6.410 MeV, may play an important role in astrophysics.

4.1.2. Trojan Horse Method measurements of the ^{18}F$(p, \alpha)^{15}$O cross section. The THM is particularly suited to investigate reactions induced by unstable nuclei since the problem of the signal-to-noise ratio is particularly severe. Indeed, in addition to the Coulomb barrier reducing the cross section to low values, the beam intensities that are usually available can be as small as 10^6 particles per second, thus making the reaction yield vanishingly small at energies typical of explosive environments such as classical novae—of the order of hundreds of keV. Another issue is the availability of suitable beam energies for the investigation of astrophysical reactions at such energies. Even if inverse kinematics has to be used in most cases, most radioactive ion beam facilities worldwide can supply beam energies significantly larger than those needed for astrophysical studies. Instead, they meet the requirements for applying the THM where the energy necessary to break the TH nucleus and the intercluster motion also make it possible to cover the astrophysical energy region with a single beam energy. This is an important feature of the THM in the case of radioactive ion beam facilities since changing beam energies in small steps to study the excitation function is often impractical.

In the case of the ^{18}F$(p, \alpha)^{15}$O reaction, we used deuterons to transfer protons and induce the reaction of astrophysical relevance. Two experiments were performed, one at CNS-RIKEN (Japan) (67) and one at the Texas A&M Cyclotron Institute (United States) (68). The two runs provided results in good agreement with each other. As discussed at length in Reference 69, the two independent astrophysical factors were averaged to yield the recommended THM $S(E)$ (blue circles in **Figure 3**). More details can be found in the original publications (67, 68).

Given the use of radioactive ion beams, the beam spot size and the beam energy range affect the resolution on the deduced ^{18}F+p relative energy spectrum. Calculations show that the energy spread reaches 53 keV (standard deviation). Therefore, to deduce the trend of the astrophysical factor devoid of energy resolution effects, we performed an R-matrix analysis of the THM S-factor.

The procedure is discussed in detail in Reference 69; here, we summarize the main results. In **Figure 3** the best fit curve, including the effects of energy resolution, is shown as a dark gray line. It is obtained under the $(+\,+)(+\,+)$ assumption for the interference pattern, adopting the notation used in figure 3 of Reference 65, in which pairs in parentheses refer to the relative interference signs between $1/2^+$ resonances (the first pair) and $3/2^+$ resonances (the second one), as listed in **Table 1**. Also, in this calculation it is assumed that a 7-keV resonance due to the ^{19}Ne state at 6.417 MeV gives a negligible contribution while introducing the contribution of a $7/2^+$ resonance due to the ^{19}Ne state at 6.537 MeV that was observed in References 67 and 68. The resonances

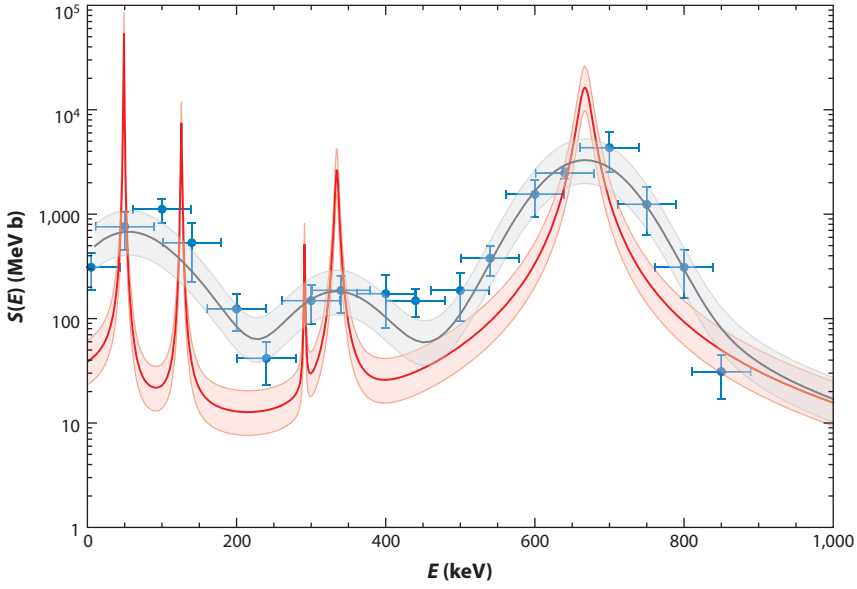

Figure 3

Trojan Horse Method (THM) astrophysical factor (*blue circles*) from the weighted average of the results of References 67 and 68. Also shown is the R-matrix fit to the experimental data including the effect of the energy resolution (*dark gray line*), equal to 53 keV (standard deviation), or devoid of energy smearing effects (*red line*). The uncertainties on the R-matrix function (expressed as one standard deviation) due to the experimental error on the THM astrophysical factor are correspondingly shown as gray and red bands. Figure adapted with permission from Reference 69; copyright 2017 The American Astronomical Society.

included in the present R-matrix analysis of THM data are shown in **Table 1**. The gray band in **Figure 3** marks the uncertainty range that stems from the fitting of the experimental data. The corresponding trend free of energy resolution effects is shown as a red band in **Figure 3** (the middle red line is the best fit curve, while the light red band highlights the uncertainty range).

Table 1 Resonance parameters from an R-matrix analysis of Trojan Horse Method data

E_{res} (keV)	E_x (keV)	J^π	Γ_p (keV)	Γ_α (keV)
−124	6,286	$1/2^+$	83.5 $fm^{-1/2a}$	11.6
29	6,440	$1/2^-$	3.8×10^{-19}	220
49	6,460	$3/2^+$	2.3×10^{-13}	0.9
126	6,537	$7/2^+$	7.1×10^{-8}	1.5
291	6,702	$5/2^+$	2.4×10^{-5}	1.2
334	6,745	$3/2^-$	2.2×10^{-3}	5.2
665	7,075	$3/2^+$	15.2	23.8
1,461	7,872	$1/2^+$	55	347

The table shows the resonance energies, the ^{19}Ne corresponding states, their spin parities, and the proton and alpha partial widths Γ_p and Γ_α (65, 69). More details can be found in References 65 and 69 and references therein. For a visualization of these data, see **Figure 3** (red line).

[a]Since this is a subthreshold state, the asymptotic normalization coefficient is given in the place of Γ_p.

While the THM data tend to rule out a significant contribution of the ^{19}Ne state at 6.417 MeV, in agreement with the lack of observation of the corresponding mirror state in the ^{15}N+α elastic scattering cross section (70), the R-matrix analysis confirms the need to introduce the 6.537-MeV state reported in References 67 and 68.

4.1.3. Consequences for classical novae investigation. From the R-matrix astrophysical factor free of energy resolution effects (red line in **Figure 3**), we calculated the ^{18}F(p, α)^{15}O reaction rate. At temperatures of interest for novae nucleosynthesis ($0.1 \leq T_9 \leq 0.5$), the THM rate is about a factor of 2 larger than the JINA REACLIB one (71), as obtained in Reference 65. To check the astrophysical consequences, we used the SHIVA code (50, 72), where the THM reaction rate was introduced (69). Specifically, we ran the code for $1.25M_\odot$ ONe white dwarfs, accreting H-rich material from the companion star at a rate of $2 \times 10^{-10} M_\odot$ year^{-1}. When adopting the THM ^{18}F(p, α)^{15}O reaction rate and the one from JINA REACLIB, we found no change in the dynamical properties but did observe differences in the chemical composition of the ejecta. In particular, a reduction of the ^{18}F yield by a factor of about 2 was obtained in the THM case. In turn, this reduction would decrease the detectability distance of the 511-keV annihilation line by γ-ray satellites by a factor of about $\sqrt{2}$, thus helping to explain the missing observation of such a γ-ray line.

4.2. The ^{7}Be(n, α)^{4}He Reaction in the Standard Big Bang Nucleosynthesis Scenario

Big bang nucleosynthesis (BBN) occurred during the time span when our Universe was able to produce nuclei: just after the baryogenesis, most probably between 1 and 20 min after the big bang, while temperature was falling from more than 10^9 K to 10^8 K. BBN has been widely studied for decades because of its importance to the understanding of the whole big bang model; together with the Galactic recession and the cosmic microwave background, BBN is one of the theory's three evidentiary mainstays. In particular, it makes it possible to probe the Universe at its earliest stages, and thus it is a valuable tool with which to constrain the physical evolution of the big bang. Information on the physical condition in the primordial era can be obtained by studying the primordial abundances of ^{2}H, ^{3}He, ^{4}He, and ^{7}Li (for a recent review, see 73 and references therein). To investigate the light element abundances and their origin and evolution, several processes must be taken into consideration besides the big bang: production by cosmic rays, stellar depletion, and nucleosynthesis. In general, understanding of the light element abundances in stars is also limited by the incomplete knowledge of many astrophysical processes (convection, microscopic diffusion, and the possible presence of additional mixing mechanisms). Moreover, light element destruction strongly depends on the adopted physical inputs and in particular on the nuclear reaction rates. An issue that has received particular attention is the discrepancy between the predicted and observed abundances of ^{7}Li in the Sun as well as in open clusters and halo or disk stars, although the complete picture regarding lithium burning in stars also includes the role of the less abundant ^{6}Li isotope (18, 74). It is important to stress that for all the other primordial isotopes (except ^{7}Li), predicted and observed abundances (in the appropriate astrophysical site) do match within uncertainties.

Despite all the efforts devoted to reduce the uncertainties, in most cases directly measured cross sections show inadequate accuracy in the energy range of interest for BBN because of intrinsic limitations, such as the presence of the Coulomb barrier for charged particle–induced reactions, or the need for neutron beams that span the energy region of astrophysical relevance. Recently, indirect measurements have been performed to overcome these difficulties, using the THM in

particular. This approach has been applied to some of the most influential reactions of the standard BBN network, such as ^{2}H(d, p)^{3}H (75–77), ^{2}H(d, n)^{3}He (75, 76), ^{3}He(d, p)^{4}He (78), and ^{7}Li(p, α)^{4}He (79, 80), and then extended to ^{7}Be(n, α)^{4}He and ^{3}He(n, p)^{3}H. These studies open up new applications of the THM to neutron-induced reactions on radioactive ion beams, thus substantially widening the use of the THM to almost all reactions that are of astrophysical interest.

4.2.1. Status of the measurements. The cross section measurements of the cosmologically relevant ^{7}Be(n, α)^{4}He reaction have been reported in different studies based on direct and indirect approaches (81–85). Even if neutron-induced reactions are not hindered by the Coulomb barrier, the reduced availability of high-luminosity and high-resolution beams at neutron facilities, as well as the need for a significant amount of radioactive ^{7}Be samples for irradiation, makes the use of indirect approaches very competitive—especially the THM. Indeed, the possibility to transfer a neutron off a deuteron makes it possible to carry out such studies at most radioactive ion beam facilities with no need to prepare and handle substantial amounts of radioactive species.

In Reference 84, the ^{7}Be(n, α)^{4}He cross section was deduced by applying the charge-symmetry hypothesis (CSH) to existing ^{7}Li(p, α)^{4}He THM data. The validity of such an approach was experimentally proved via the agreement between the direct ^{7}Be(n, α)^{4}He cross section measurements of Reference 83 and those of Reference 81 based on the CSH using an old set of ^{7}Li(p, α)^{4}He data. For the purposes of the THM, we started from the ^{7}Li(p, α)^{4}He cross section data of References 86 and 87 based on deuteron and ^{3}He breakup THM experiments. In addition, because we were interested in using the experimental data of use to the ^{7}Be(n, α)^{4}He investigation, we considered only some of the available data. In particular, because of the mass difference in the two ^{7}Li+p and ^{7}Be+n entrance channels, a difference of 1.644 MeV was present between the center-of-mass energies covered in the two cases. For this reason, only the ^{7}Li(p, α)^{4}He THM cross section data, $\sigma_{p\alpha}$, covering a center-of-mass energy $E_{\mathrm{Li}+p} > 1.644$ MeV, were taken into account. The THM data were converted to the $\sigma_{n\alpha}$ of the ^{7}Be(n, α)^{4}He channel via the following relation:

$$\sigma_{n\alpha} \cdot \frac{E_{\mathrm{Li}+p} - 1.644}{P^n_{l=1}(E_{\mathrm{Li}+p} - 1.644)} = \sigma_{p\alpha} \cdot \frac{E_{\mathrm{Li}+p}}{P^p_{l=1}(E_{\mathrm{Li}+p})}, \qquad 52.$$

where $P^n_{l=1}$ and $P^p_{l=1}$ represent the penetrability for the neutron channel and the proton channel, respectively (84). The result shows fair agreement with the data from References 81 and 83 and has the advantage of producing a cross section measurement right in the BBN energy region. The good agreement once again shows the validity of our assumption, as was previously done in Reference 81. Then, the THM reaction rate was used as input in the evolutionary code described in Reference 80 to derive the primordial ^{2}H, ^{3,4}He, and ^{7}Li abundances. Besides the above-mentioned agreement for deuterons and helium isotopes, a marked disagreement appears for lithium, and thus the "Li problem" remains open in cosmology.

4.2.2. Trojan Horse Method measurements. The THM experiment to determine the ^{7}Be(n, α)^{4}He cross section is discussed in Reference 85. The ^{2}H(^{7}Be,$\alpha\alpha$)p three-body reaction was measured at the EXOTIC facility (88) of INFN–Laboratori Nazionali di Legnaro using a 20.4-MeV ^{7}Be beam impinging on a CD_2 target with a thickness of 400 μg cm^{-2}. In the QF ^{2}H(^{7}Be,$\alpha\alpha$)p process, the deuteron was used as a TH nucleus because of its relatively low binding energy (∼2.2 MeV) and the dominance of the S-wave in the pn intercluster motion (89). In the ^{2}H+^{7}Be interaction, the deuteron undergoes its breakup into a neutron (participant) and proton (spectator). The EXOTIC facility is devoted to the in-flight production of light weakly bound radioactive ion beams, and unstable ^{7}Be beams have been produced previously (see, e.g., 90). For the

experiment described in Reference 85, ^{7}Li ions (150–200 pnA) were delivered by the LNL-XTU Tandem accelerator onto a H_2 gas target to induce the ^{7}Li(p, n)^{7}Be reaction ($Q = -1.64$ MeV). The gas target consisted of a 5-cm-long gas cell doubly walled with 2.2-μm-thick Havar foils, and it was filled with 1 bar H_2 gas at cryogenic temperatures (90 K), corresponding to a target thickness of about 1.35 mg cm^{-2}. The ^{7}Be secondary beam was separated from the ^{7}Li scattered beam and from other contaminants by means of a 30°-bending magnet, a Wien filter, slit settings, and collimation systems located at suitable positions along the beam line (90). At the end of the beam line, an intensity of 5×10^5 to 8×10^5 pps, a purity of about 99%, a beam spot of about 9 mm (FWHM), and an energy spread of about 1 MeV (FWHM) were measured.

The two emerging α particles were detected at the QF angle pairs—that is, the angle pairs at which the spectator maintains the same momentum it had inside the deuteron before its breakup. The kinematic quantities of the undetected proton were reconstructed via momentum and energy conservation laws (8).

The ^{2}H(^{7}Be,$\alpha\alpha$)p channel selection was accomplished by reconstructing the experimental Q value spectrum once the α particles had been selected through the standard ΔE-E technique. The experimental peak is centered at ∼16.76 MeV, in agreement with the theoretical one of 16.765 MeV, with a FWHM of about 2 MeV.

The trend of the momentum distribution for the pn intercluster motion inside deuterons was used to select the QF reaction mechanism. The agreement shown in Reference 85 unambiguously marked the presence of the QF reaction mechanism and therefore allowed us to proceed further in the extraction of the ^{7}Be(n, α)^{4}He binary cross section. Thus, the two-body reaction cross section was properly evaluated, taking into account HOES effects as well as the normalization to available direct data from References 81–83.

The HOES differential cross section was extracted and converted to the OES cross section including the centrifugal barrier effects based on the $l = 1$ orbital angular momentum, which arises from the broad P-wave ^{7}Be+n resonances at ^{8}Be excitation energies around 20 MeV (85). The results of this THM investigation are shown in **Figure 4** with the corresponding statistical uncertainties. The THM data span a broad energy region (i.e., from ∼30 keV up to ∼2 MeV), providing a cross section in the region of interest for BBN. The THM data nicely overlap with the direct data from Reference 83 and, at lower energies, with the data derived via the CSH in Reference 81. Additionally, the THM results agree with the data derived in Reference 84. **Figure 4** also shows an evaluation of the total S-wave component for the observed reaction as derived in Reference 82 and the ENDF/B-VII.1 evaluation from Reference 91. Even if the uncertainties affecting the experimental data are quite large, in some energy regions, such as close to the 1- and 3-MeV resonances, the ENDF/B-VII.1 calculation deviates from the experimental data present in the literature, while its overall trend qualitatively agrees with them. The derived reaction rate shows good agreement with that of Reference 81 with improved uncertainties at BBN energies. Although the primordial ^{7}Li abundance evaluated via the code used in Reference 80 remains far from the observed one, the THM investigation provides a reduced uncertainty on the corresponding reaction rate.

4.3. The ^{19}F(α, p)^{22}Ne Reaction and Fluorine Destruction in Evolved Stars

The ^{19}F(α, p)^{22}Ne reaction has an important astrophysical role in helping us understand the destruction of ^{19}F in multiple astrophysical contexts. In fact, the pathways in which ^{19}F is produced are quite clear, while there is much uncertainty regarding its destruction. A suggested path in asymptotic giant branch (AGB) stars is the ^{19}F(α, p)^{22}Ne reaction (92, 93), whose importance critically depends on the environment. In an He-rich environment, such as the convective envelope near the He shell, this reaction constitutes the main channel for ^{19}F burning in such contexts. It is

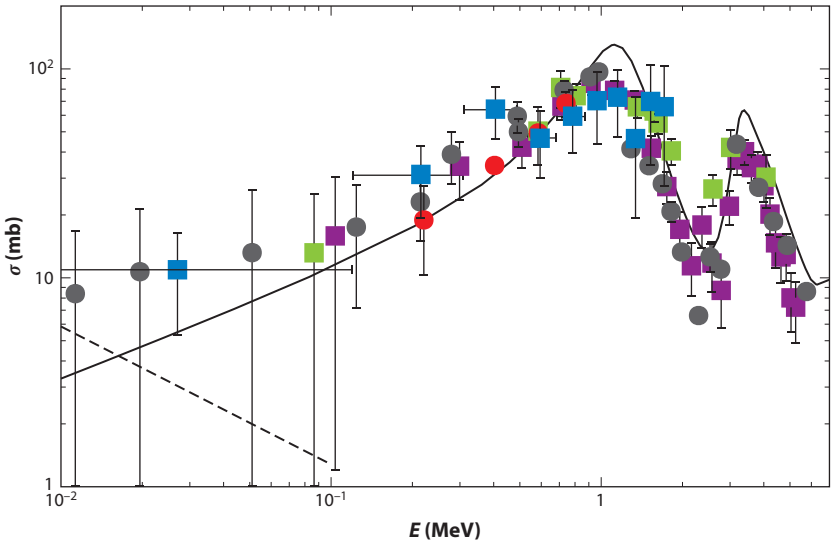

Figure 4

The ^{7}Be$(n, \alpha)^{4}$He cross section measurements as reported in Reference 85, including results from References 81 (*gray circles*), 83 (*red circles*), 84 (*purple* and *green squares*), and 85 (*blue squares*). The dashed black line indicates the total S-wave component for the observed reaction as derived in Reference 82; the solid black line indicates the ENDF/B-VII.1 evaluation from Reference 91. Figure adapted with permission from Reference 85; copyright 2019 The American Astronomical Society.

therefore important to know the reaction rate for ^{19}F$(\alpha, p)^{22}$Ne even though it is not measured in the energy range of astrophysical interest. In fact, direct measurements of the cross section at the Gamow energy region for a stellar temperature of $T = 8 \times 10^8$ K should be performed at energies in the center-of-mass reference frame between 0.4 and 0.8 MeV, while the lowest available energy for such a measurement is at 1.1 MeV (94), corresponding to ~660 keV in the center of mass.

The proposed R-matrix fit accounts for the observed resonances, and extrapolation of the cross section was performed to deduce the low-energy behavior. Nevertheless, the reduced widths γ_α of the involved resonances were merely estimated, and a more precise determination would be necessary. Thus, an experimental measurement is needed, possibly in the Gamow energy range, to better understand ^{19}F burning in an AGB environment proceeding through this reaction. Such a measurement has been provided by the THM.

The reaction was studied using a ^{6}Li nucleus as a TH nucleus, and kinematic conditions were selected in which the ^{6}Li(^{19}F,p^{22}Ne)^{2}H reaction proceeds mainly via QF breakup (95). We would like to highlight that in this case, the spectator was a charged particle—a deuteron in particular. Nevertheless, previous validity tests clearly demonstrated that the THM obeys the pole invariance; that is, the cross section of the binary reaction is independent of the spectator that is used. In particular, it was proved in different experimental runs that the method is perfectly coherent independent of the spectator cluster, even in the case of neutral versus charged spectators (87, 96) (for a recent review of the topic, see 10).

The experiment was performed at the Ruđer Bošković Institute (Croatia) using a 6-MeV ^{6}Li beam. The α cluster behaved as a participant to the binary process, while p acted as a spectator to the QF reaction. As discussed above, the beam energy was chosen to measure the ^{19}F$(\alpha, p)^{22}$Ne cross section in the energy region of interest for astrophysics. A complete description of the experimental procedure as well of the data analysis performed is reported in References 12 and 95.

Table 2 Energies of the ^{23}Na states investigated in the ^{19}F(α, p)^{22}Ne reaction

E_R (MeV)	E_{CM} (MeV)	J^π	γ_α (MeV$^{1/2}$)	γ_p (MeV$^{1/2}$)	$\gamma_{p'}$ (MeV$^{1/2}$)
10.477	0.01	$3/2^+$	0.001	0.124	0.342
10.616	0.149	$5/2^+$	0.005	0.087	0.327
10.823	0.356	$3/2^+$	0.007	0.131	0.417
10.907	0.44	$5/2^+$	0.001	0.054	0.350
10.972	0.505	$5/2^+$	0.009	0.044	0.184
10.994	0.527	$3/2^+$	0.005	0.011	0.079
11.038	0.571	$3/2^+$	0.003	0.049	0.179
11.109	0.642	$5/2^+$	0.012	0.016	0.096
11.273	0.806	$3/2^+$	0.003*	0.045	0.279
11.280	0.812	$3/2^+$	0.003*	0.127	0.320
11.303	0.836	$3/2^+$	0.003*	0.105	0.148

The measured centroid is reported in the first column; also shown are the J^π of the levels and the reduced widths arising from the R-matrix fit discussed in Reference 95. Values marked with asterisks are from Reference 94.

In this case, the formalism discussed in Section 3.2.3 was adopted—in particular, Equation 50 to deduce the reduced γ widths from the THM cross section. After selecting the QF mechanism according to the THM prescriptions, angular distributions as well as excitation function were extracted and analyzed through the modified R-matrix approach and then compared, after normalization, with direct data from Reference 94. Many resonant levels were studied (see **Table 2**). A nice agreement between indirect and direct data showed up in the overlap energy region above the Coulomb barrier, and the reaction rate was thus calculated.

In **Figure 5** this reaction rate, as reported in Reference 95, is shown together with its uncertainties arising from experimental data and compared with the rate based on direct data (94). In the astrophysical temperature range $0.2 \leq T_9 \leq 0.5$, a clear enhancement of the reaction rate is evident up to a factor of five. The astrophysical impact of such a measurement is discussed in Reference 12.

4.4. The ^{3}He(n, p)^{3}H Reaction in the Standard Big Bang Nucleosynthesis Scenario

The THM has proved decisive in measuring several neutron-induced reaction cross sections, some of which are of astrophysical relevance (97–101). One reaction that has been extensively studied recently is the ^{3}He(n, p)^{3}H process. This process is important in BBN and has an impact on the primordial ^{3}He and ^{7}Li abundances (see 80 and references therein). Consequently, its reaction rate can be related to the primordial lithium problem, thus helping us find a possible nuclear solution to it. At temperatures corresponding to BBN, the reaction rate is linked to the cross section in the energy range 0.03 MeV $\leq E_{CM} \leq$ 0.3 MeV. The first studies of this reaction were performed in the range 0.1 MeV $\leq E_{CM} \leq$ 30 MeV using a neutron beam (102). Errors were around 30%. Other measurements, which were more focused at lower energies, were conducted in Reference 103 (direct measurement in the range $0.1 \leq E_{CM} \leq 1$ MeV), Reference 104 (inverse measurement with larger uncertainties), and Reference 105 (direct measurement in the range 0.3 MeV $\leq E_{CM} \leq$ 1.1 MeV). The most recent data in a wide energy range can be found in Reference 106. Reaction rates were then calculated for astrophysical applications in References 107 and 108, which show a similar trend at the relevant temperatures, while the reaction rate calculated in Reference 109

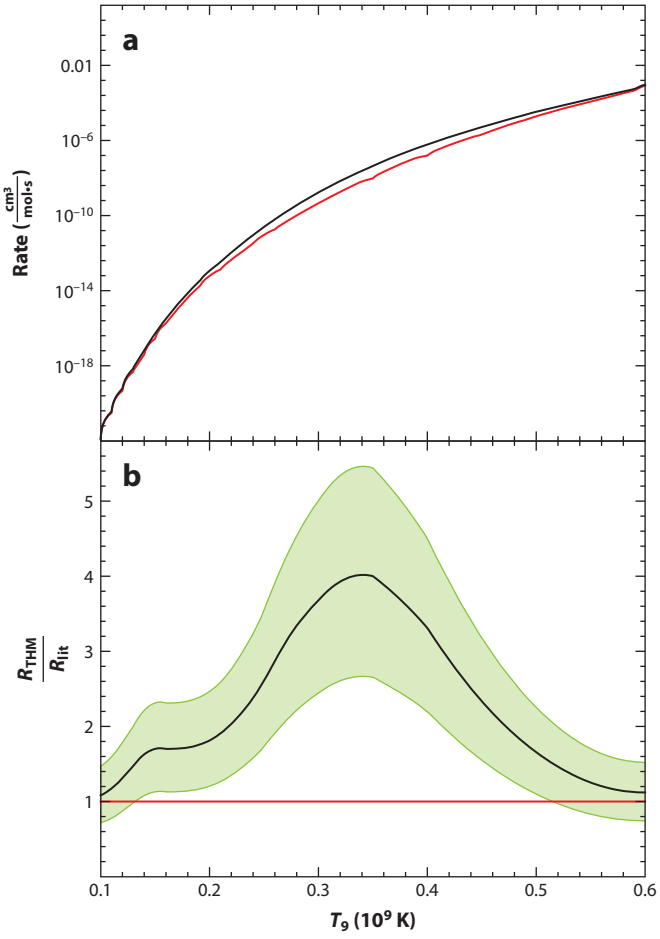

Figure 5

(*a*) Trojan Horse Method (THM) reaction rate for the $^{19}F(\alpha, p)^{22}Ne$ reaction (*black line*) compared with the one calculated in Reference 94 based on direct data (*red line*). (*b*) Ratio between the THM and calculated (94) rate. The green area is defined by the uncertainties in the THM data. Figure adapted with permission from Reference 95; copyright 2017 The American Astronomical Society.

is sensitively higher. In the energy range of interest, the existing data are therefore sparse; most of these data were measured more than 50 years ago after facing tough experimental challenges, which resulted several times in errors as high as 30% (see **Figure 6**).

To extract the total reaction cross section, the $^2H(^3He,pt)H$ process was investigated in QF kinematics to retrieve information on the $^3He(n, p)^3H$ reaction in the Gamow energy range. In this case, the TH nucleus *d* breaks up into its constituents, *n* (participant) and *p* (spectator). The experiment was performed using a ^3He beam delivered at a total kinetic energy of 9 MeV by the FN Tandem accelerator at the Nuclear Physics Laboratory, University of Notre Dame (United States).

Data analysis was performed according to the prescriptions of the THM and is exhaustively discussed in Reference 110. After the selection of the QF process that was performed by means of a detailed study of the spectator momentum distribution, the binary cross section was extracted

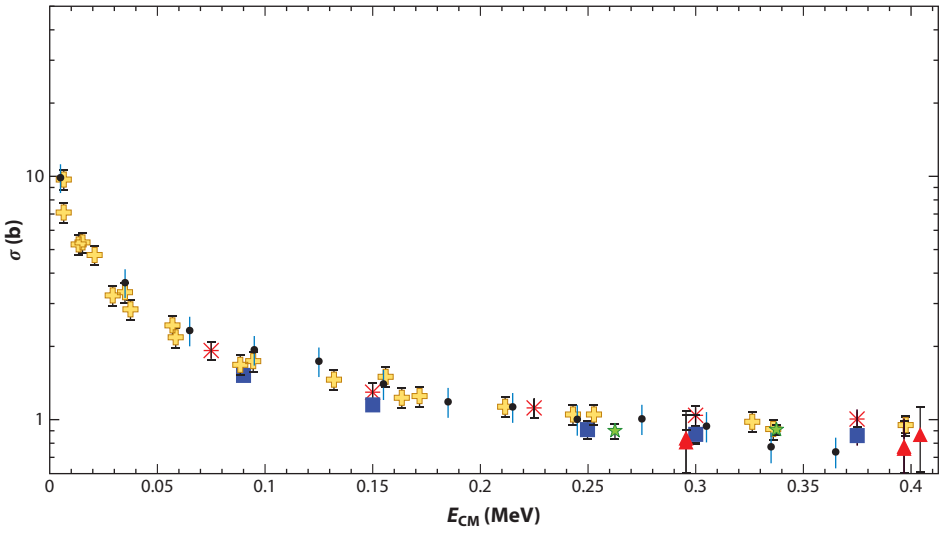

Figure 6

Total bare nucleus cross section for the ^{3}He(n, p)^{3}H reaction deduced via the Trojan Horse Method (*black circles*) after normalization to the available direct data from References 103 (*blue squares*), 104 (*yellow crosses*), and 106 (*red stars*). Data from References 102 (*red triangles*) and 105 (*green stars*) are also shown. The displayed error bars account for statistics and normalization. Figure adapted from Reference 110 with kind permission of *The European Physical Journal* (*EPJ*).

in the energy range $0.03 \leq E_{CM} \leq 0.3$ MeV. This cross section is shown in **Figure 6** along with the different data sets available in the literature for comparison. The cross section, as required by the THM, was normalized to the direct data from References 103, 104, and 106 in the energy range $0.2 \leq E_{CM} \leq 0.35$ MeV. A remarkable agreement shows up in the whole energy range, with small deviation (around 10%) in the energy region important for astrophysics. Statistical errors as well as normalization errors were fully taken into account, yielding an average 10% relative error for the cross section extracted via the THM. Regarding the error on the quantities contributing to E_{CM}, we apply the error propagation with an uncertainty on the experimentally measured energies for protons and tritons, E_p and E_t, of 0.8% and an error on the respective angles of $\Delta\theta_p \approx \Delta\theta_t \approx 0.15°$.

Further analysis is in progress to extend the measurement to higher energies through the use of additional data sets. This will allow calculation of the reaction rate in an extended energy interval and evaluation of the astrophysical impact of this measurement.

4.5. The ^{12}C+^{12}C Fusion at Astrophysical Energies

The ^{12}C+^{12}C fusion is a crucial process in different scenarios with carbon-rich environments. In particular, it determines the late evolution and the nucleosynthesis of intermediate-mass and massive stars ($\geq 8M_\odot$) (111); it influences the lower mass limit for carbon ignition, which separates the progenitors of white dwarfs, novae, and type Ia supernovae from those of core-collapse supernovae, neutron stars, and stellar-mass black holes. It is considered the ignition reaction of type Ia supernovae and superbursts, in particular if resonances are found to contribute in the Gamow peak (112). Moreover, it influences the weak component of the s-process, which produces the elements between Fe and Sr. Quiescent carbon burning takes place from 0.8 to 1.2 GK, a range that corresponds to center-of-mass sub-Coulomb energies from 1 to 3 MeV where the cross section of this process falls rapidly below the nanobarn range. This fact explains why the cross section has

never been measured below a center-of-mass energy of 2 MeV. The compound nucleus ^{24}Mg is formed at an excitation energy above the ^{12}C+^{12}C decay threshold. Alpha particles, protons, and neutrons are the dominant evaporation channels and lead, respectively, to ^{20}Ne, ^{23}Na, and ^{23}Mg, which can also be produced in excited bound states. Below 2.5 MeV, there is not enough energy to feed ^{23}Mg even in its ground state, and the α and p channels are the only relevant ones.

4.5.1. The Trojan Horse Method ^{14}N+^{12}C experiment. The ^{12}C+^{12}C fusion cross section at astrophysical energies was determined from the measurement of the ^{12}C(^{12}C,α)^{20}Ne and ^{12}C(^{12}C,p)^{23}Na reactions via the THM applied to the ^{12}C(^{14}N,α^{20}Ne)^{2}H and ^{12}C(^{14}N,p^{23}Na)^{2}H three-body processes in QF kinematics with ^{2}H from the ^{14}N spectator to the ^{12}C+^{12}C reactions (14). The experiment was performed at the INFN–Laboratori Nazionali del Sud in Catania, Italy. A ^{14}N beam accelerated at 30 MeV by the SMP Tandem was delivered onto a 100-μg cm^{-2} C target. The ejectile of the two-body reactions (either α or p) was detected in coincidence with the spectator d particle by means of silicon telescopes at either side of the beam directions covering angular regions optimized for the QF kinematics of the breakup process of interest. Additional experimental details can be found in Reference 14.

The occurrence and dominance of the QF mechanism in all cases were indicated by the agreement within 5% between the shape of the experimental momentum distribution (in the range 30–80 MeV/c) and that obtained from the Woods-Saxon ^{12}C+d bound state potential with standard geometric parameters $r_0 = 1.25$ fm, $a = 0.65$ fm, and $V_0 = 54.428$ MeV, adjusted to give the experimental ^{12}C+d binding energy in ^{14}N. Agreement with the theoretical shape of the momentum distribution calculated in the framework of the DWBA was recently demonstrated in the experimental range of 30 to 80 MeV/c. This important result will be presented in a forthcoming paper (A. Tumino et al., manuscript in preparation). It provides further validation that in the phase space region populated in the experiment, it is possible to apply the PWIA to extract the cross section for the binary system. The PWIA is convenient because of the simple link to the three-body cross section—a link that is ensured in the modified R-matrix approach by the presence in the total PWIA amplitudes of the same matrix elements as in the OES binary reaction cross section (see Equation 50).

After completion of data analysis (14), the two-body cross section of astrophysical relevance was extracted for four channels: ^{20}Ne+α_0, ^{20}Ne+α_1, ^{23}Na+p_0, and ^{23}Na+p_1. A modified one-level many-channel R-matrix analysis was carried out including the ^{24}Mg states reported in Reference 14. According to the results of Reference 113 at $E_{CM} \leq 3$ MeV, and monitoring the decrease of the penetration factors for the relevant states, the fraction of the total fusion yield from α and p channels other than $\alpha_{0,1}$ and $p_{0,1}$ was neglected in the modified R-matrix analysis with estimated errors at $E_{CM} < 2$ MeV lower than 1% and 2% for the α and p channels, respectively. The resonance structure observed in the excitation functions is consistent with ^{24}Mg resonance energies reported in the literature.

The THM reduced widths thus entered a standard R-matrix code, and the S-factors for the four reaction channels were determined. The results are shown in **Figure 7** in terms of the total modified S-factor, $S(E)^*$ (114).

The E_{CM} range between 2.5 and 2.63 MeV of the ^{20}Ne+α_1 channel was chosen for normalization to direct data because in this range the available data (115–118) are the most accurate of those overlapping with THM data. The resulting normalization error is 5%. Existing direct data below $E_{CM} = 4$ MeV are also shown in **Figure 7**. Except for the data from References 115, 122, and 123, their low-energy limit is fixed by background due to hydrogen contamination in the targets. Disregarding these cases, agreement between THM and direct data is apparent within the experimental errors except for the direct low-energy limit around 2.14 MeV, where THM data

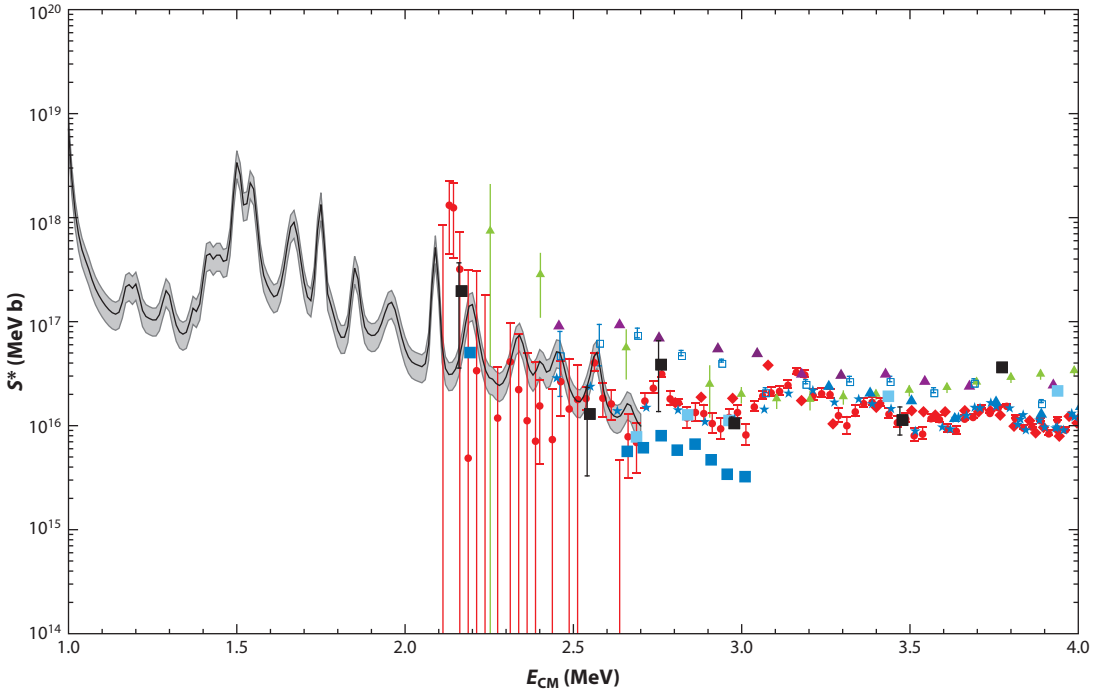

Figure 7

Trojan Horse Method total S^*-factor (*black line*). The gray band represents the region spanned by R-matrix calculations with lower and upper values of the resonance parameters. Available direct data in the E_{CM} range below 4 MeV are indicated by red circles (115), purple triangles (116), open blue squares (117), blue stars (118), blue triangles (119), red diamonds (113), green triangles (120), solid light blue squares (121), black squares (122), and solid dark blue squares (123).

do not confirm the claim of a strong resonance; rather, they indicate a nearby one at 2.095 MeV that is about one order of magnitude less intense in the $^{20}Ne+\alpha_1$ channel and of similar intensity in the $^{23}Na+p_1$ channel. The present result is in agreement with spectroscopy studies (124, 125) with a deep at 2.14 MeV and no particularly strong α state around 2.1 MeV. Further agreement is found with data down to $E_{CM} = 2.15$ MeV from Reference 126 for the $^{12}C(^{12}C,p_{0,1})^{23}N$ reactions. Our result is also consistent within experimental errors with the total $S(E)^*$ from recent results (121–123), though the upper limit for the proton channel from Reference 123 below $E_{CM} = 3$ MeV is significantly lower than the other results. A theoretical reanalysis of THM data (127) that applied a theory based on the DWBA resulted in much lower $S(E)^*$ values by up to four orders of magnitude. However, the convergence of the calculations involving a transfer to an unbound system is not obvious, and a careful examination shows that, on top of other things, the numeric stability of the proposed theory is not guaranteed. Thus, the results are very sensitive to details of the model space, and the calculated trend of the THM $S(E)^*$ is questionable. Recent theoretical calculations within the framework of a time-dependent Hartree-Fock-based classical model using the Feynman path integral method (128) have included some of the low-energy resonances in the E_{CM} region of the THM data, leading to $S(E)^*$ values in agreement with what was shown in the THM experiment (14). This work highlights the important role of resonances in shaping the trend of $S(E)^*$, an aspect neglected in previous attempts (109, 114, 129–132) to extrapolate $S(E)^*$ at astrophysical energies.

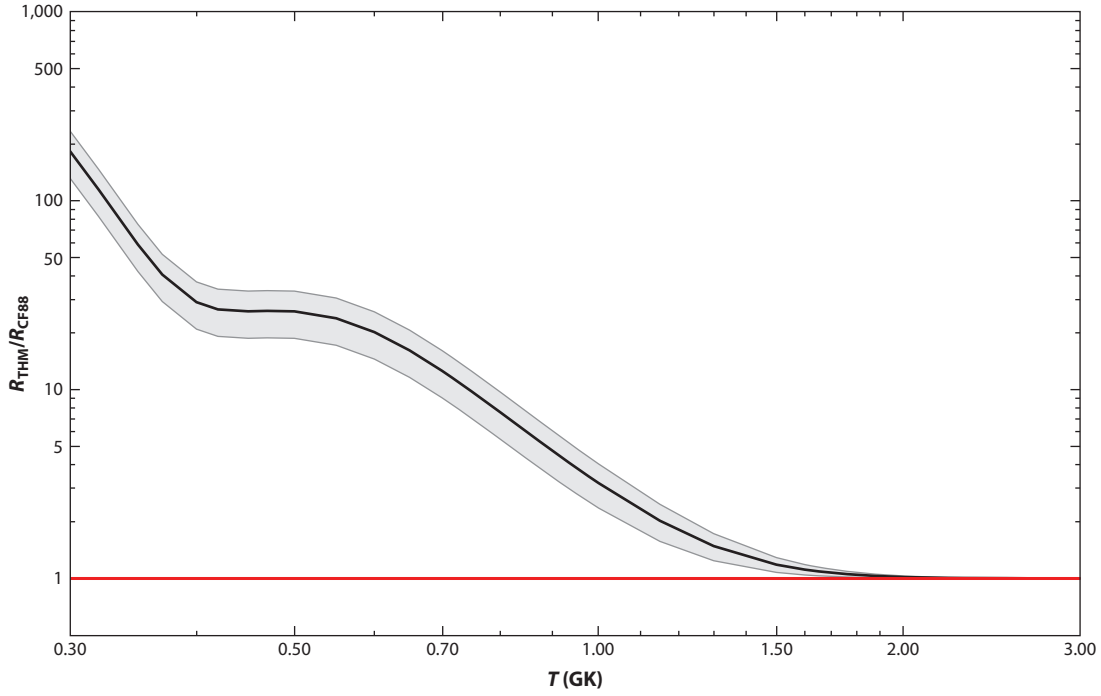

Figure 8

Ratio between the total Trojan Horse Method (THM) $^{12}C+^{12}C$ reaction rate R_{THM} (*black line*) from Reference 14 and the reference rate R_{CF88} (*red line*) from Reference 109. The gray shading defines the region spanned considering the $\pm 1\sigma$ uncertainties. Figure adapted from Reference 133 with kind permission of Società Italiana di Fisica; copyright 2019 Italian Physical Society.

4.5.2. Consequences for astrophysics. **Figure 8** shows the THM reaction rate at the relevant temperatures divided by the reference rate from Reference 109. Below 2 GK, it increases from a factor of 1.18 at 1.2 GK to a factor of more than 25 at 0.5 GK. As for the hydrostatic carbon burning regime (0.6–1.2 GK), the rate increase lowers the temperatures and densities at which ^{12}C ignites in massive stars. According to the stellar modeling reported in Reference 134, for core carbon burning of a $25M_{\odot}$ star, the ignition temperature and density would undergo a decrease down to 10% and 30%, respectively. The increase at 0.5 GK, which is mainly due to the resonant structure around $E_{CM} = 1.5$ MeV, meets the fiducial value conjectured in Reference 112 to reduce down to a factor of two the theoretical superburst ignition depths in accreting neutron stars for a realistic range of crust thermal conductivity and core Urca neutrino emissivity. This change is compatible with the superburst ignition depths inferred from observations. Thus, carbon burning can trigger superbursts. Recently, the impact of the new carbon fusion cross sections on type Ia supernovae was investigated in Reference 135. Their progenitors are yet to be fully understood. One popular scenario is the double-degenerate (DD) scenario, which attributes type Ia supernovae to white dwarf binary mergers. The resonance contribution results in a decrease of the carbon burning ignition temperature. Thus, accretion-induced collapse occurs more easily and increases the birth rate of Galactic neutron stars with the contribution of the DD scenario to the type Ia supernovae rate becoming even smaller. Effects of the THM reaction rate on the upper bound for the masses of the progenitors of CO white dwarfs (M_{up}) and the lower bound for the masses of the progenitors of normal type II supernovae (M^*) have been analyzed in Reference 136. In particular, M_{up} is reduced from 8 to $7.5M_{\odot}$, while M^* approaches $10M_{\odot}$.

5. CONCLUSIONS

The THM is a well-established tool to help overcome unwelcome physics phenomena, such as Coulomb/centrifugal suppression and electron screening effects, in the study of astrophysically relevant reactions. In this review, we have presented its theoretical formulation in a comprehensive and instructive way, describing its historical developments and adaptation to experimental needs. Recent applications have been discussed, which open up future prospects for experiments using the THM with heavier stable nuclei as well as with radioactive ion beams. In particular, the use of heavier TH nuclei, such as ^{13}C, ^{14}N, ^{20}Ne, ^{23}Na, and ^{26}Mg, will enable assessment of important reactions that play a role in late evolutionary stages of massive stars in terms of energy generation and production of heavy elements. As an example, the last two mentioned nuclei can transfer ^{22}Ne to investigate the ^{22}Ne$(\alpha, n)^{25}$Mg reaction, the main neutron source in the so-called weak s-process (137, 138). Reliability tests of such systems as future TH nuclei are underway to design the next generation of experiments. The THM will also play a major role in the determination of the reaction rates using deuterons as sources of virtual neutrons to study neutron-induced reactions on short-lived radioactive ions. As more rare isotope beams become available around the world, nuclear reactions—for instance, those involved in the r-process (139)—will be studied via the THM. In short, the THM is an incredibly versatile tool that is paving new paths to clarify the nuclear physics that shapes the Universe.

SUMMARY POINTS

1. The Trojan Horse Method (THM) offers a unique probe with which to determine the cross section of a two-body reaction at astrophysical energies by measuring a suitable transfer reaction with three bodies in the final state in quasi-free (QF) kinematics and at energies above the Coulomb barrier. Successful application of this method requires the selection of suitable Trojan Horse (TH) nuclei that have a prominent cluster structure to transfer (e.g., nucleons, deuterons, α particles). The method can be applied to charged particle reactions, either resonant or nonresonant, as well as to neutron-induced reactions, involving both stable and radioactive ion beams.
2. Nuclear reaction theory has progressed to improve our confidence regarding a precise relation between two- and three-body cross sections. It has helped clarify the factorization of the cross sections of two- and three-body reactions. This factorization is linked to the unraveling of the two vertices shown in **Figure 1**. The theory exploits the fact that the reactions are dominated by peripheral processes where only the asymptotic part of the bound state wave functions is relevant. The peripherality and QF scattering constraints determine the selection of the kinematics in the experiments.
3. Two examples of reactions involving unstable nuclei have been reported: ^{18}F$(p, \alpha)^{15}$O and ^{7}Be$(n, \alpha)^{4}$He. Both reactions are involved in explosive scenarios—the former in the case of classical novae thermonuclear runaways and the latter in standard big bang nucleosynthesis. Two key elements for nucleosynthesis are destroyed, ^{18}F and ^{7}Be, the latter of which is especially important as a progenitor of ^{7}Li. The ^{18}F isotope could be responsible for a 511-keV annihilation line following β^+ decay, which is presently not observed by satellite-borne instruments. THM measurement suggests a stronger burning rate, which helps to explain the lack of observations. A ^{7}Be$(n, \alpha)^{4}$He THM study aimed to shed light on the well-known discrepancy between primordial lithium abundance measurements

and model predictions. It represents the first test study for future investigations of reactions involving neutrons and unstable nuclei, whose measurement is possible only by indirect means.

4. The ^{3}He(n, p)^{3}H reaction is also related to the primordial lithium problem. The THM equivalent measurement shows, within the experimental errors, a satisfying agreement between direct and inverse reaction data from previous experiments, making it possible to access the low astrophysical energies and to carry out neutron-induced reactions at any laboratory as a much cheaper alternative to expensive neutron facilities.
5. The ^{19}F(α, p)^{22}Ne reaction is the main fluorine destruction channel in He-rich environments, such as the convective envelope near the He shell in asymptotic giant branch (AGB) stars. The ^{19}F isotope is especially important since its abundance may be used to constrain the physical conditions inside AGB stars and, therefore, to shed light on the s-process. This knowledge is essential since r-process yields are based on those of the s-process, creating a link with the growing field of multimessenger astronomy. The THM measurement of the ^{19}F(α, p)^{22}Ne astrophysical factor extends to astrophysical energies, leading to a reaction rate increased by as much as a factor of four with respect to the previously published values that relied on extrapolations.
6. The ^{12}C+^{12}C fusion is crucial in any scenario in carbon-rich environments. It determines, for instance, the late evolution and nucleosynthesis of stars with masses $\geq 8M_{\odot}$, influences the mass limit for carbon ignition, and constrains type Ia supernovae and superburst models. In a THM measurement, ^{14}N was used to transfer a ^{12}C nucleus, and the ^{12}C(^{12}C,$\alpha_{0,1}$)^{20}Ne and ^{12}C(^{12}C,$p_{0,1}$)^{23}Na cross sections were deduced at astrophysical energies. They exhibit several resonances that are responsible for a very large increase in the reaction rate at relevant temperatures. Implications regarding massive stars, superburst ignition, and type Ia supernovae are under scrutiny.

FUTURE ISSUES

1. A proper theoretical description of reactions is the basis for the application of the THM. Although it has advanced significantly, there is still ample room for improvement. Present formulations cannot coherently account for distortion and coupled-channel effects. These complications harm the desired connection between the cross sections of the THM $2 \rightarrow 3$ reactions and the $2 \rightarrow 2$ reactions of astrophysical interest. These uncertainties could affect the energy dependence of the cross sections extracted from the experiments. In particular, the accuracy of the factorization of the reaction cross section has to be checked in comparison to that of more elaborate approaches that consider the three-body nature of the final states and fully take into account the final-state interactions between nuclei. As a consequence, experiment and data analysis have to be performed in a very careful and selective way, imposing strict kinematic conditions and using only a fraction of the available data to meet the specific requirements of the factorization of the reaction cross section while still obtaining sufficient statistics. A consistent description of reactions and nuclear structure (e.g., using more microscopic approaches) is also necessary. Further advancements in theory are presently being evaluated that aim

to incorporate in a coherent way distorted waves in a process described as a transfer to the continuum.

2. TH experiments require beam energies typical of small-scale accelerators, such as Tandems. The development of nuclear astrophysics and in particular the need for indirect methods have ushered in a new era for such accelerators that were about to fall into disuse, as already happened in several parts of the world. The nuclear needs for astrophysics have in many occasions shown the lack of solid spectroscopic studies for several nuclei. The revival of this low-energy physics is an important task that is supported in all nuclear physics long-range plans.
3. Angular resolution is a key feature in the application of the THM. Reactions populating medium-heavy compound systems show a rich pattern of closely spaced resonances that have to be detected and measured individually. New high-granularity detection systems, with low thresholds and allowing for particle identification, are presently under development to increase the accuracy of the method. A theoretical description of these systems that employs statistical approaches (e.g., Hauser-Feshbach theory) cannot be applied to calculate their reaction cross sections because the basic hypotheses are not fulfilled.
4. Intercluster motion represents a key ingredient when selecting a given TH nucleus. To date, only nuclei with a dominant S-wave intercluster motion have been chosen for TH application (e.g., ^{2}H, ^{3}He, ^{6}Li, ^{9}Be, ^{14}N). To extend the range of applicability of the method, P-wave intercluster motion configurations need to be selected, and focused studies are expected in the near future.
5. Advanced burning stages in stars call for the investigation of reactions that involve heavy nuclei. Therefore, it is desirable to test alternative TH nuclei to transfer the corresponding systems. An example is the ^{16}O+^{16}O fusion reaction. Such studies must be carried out in parallel from the experimental and theoretical points of view because these systems may be deformed in their ground state, for instance, making it necessary to apply customized nuclear models.

DISCLOSURE STATEMENT

The authors are not aware of any affiliations, memberships, funding, or financial holdings that might be perceived as affecting the objectivity of this review.

ACKNOWLEDGMENTS

C.A.B. acknowledges support from US Department of Energy grant DE-FG02-08ER41533. L.L. and S.R. acknowledge "Programma ricerca di ateneo UNICT 2020-22 linea 2" and "Starting grant 2020" from the University of Catania.

LITERATURE CITED

1. Assenbaum HJ, et al. *Z. Phys. A* 327:461 (1987)
2. Strieder F, et al. *Naturwissenschaften* 88:461 (2001)
3. Fiorentini G, et al. *Z. Phys. A* 350:289 (1995)
4. Spitaleri C, et al. *Nucl. Phys. A* 719:C99 (2003)
5. Tumino A, et al. *Few-Body Syst.* 54:869 (2013)

6. Tribble R, et al. *Rep. Prog. Phys.* 77:106901 (2014)
7. Tumino A, et al. *Few-Body Syst.* 54:745 (2013)
8. Spitaleri C, et al. *Eur. Phys. J. A* 52:77 (2016)
9. Spitaleri C, et al. *Eur. Phys. J. A* 55:161 (2019)
10. Pizzone RG, et al. *Eur. Phys. J. A* 56:283 (2020)
11. Rapisarda GG, et al. *Eur. Phys. J. A* 54:189 (2018)
12. D'Agata G, et al. *Astrophys. J.* 860:61 (2018)
13. Lamia L, et al. *Astrophys. J.* 811:99 (2015)
14. Tumino A, et al. *Nature* 557:687 (2018)
15. Baur G. *Phys. Lett. B* 178:135 (1986)
16. Baur G. *Nucl. Energy* 25:183 (1987)
17. Shapiro IS. *Sov. Phys. Usp.* 10:515 (1968)
18. Tumino A, et al. *Phys. Rev. C* 67:065803 (2003)
19. La Cognata M, et al. *Astrophys. J.* 708:796 (2010)
20. Thompson IJ. *Comp. Phys. Rep.* 7:167 (1987)
21. Perey CM, Perey FG. *At. Data Nucl. Data Tables* 17:1 (1976)
22. Newton RG. *Scattering Theory of Waves and Particles*. Berlin: Springer (1982)
23. Typel S. *Eur. Phys. J. A* 56:286 (2020)
24. Jain M, Roos PG, Pugh HG, Holmgren HD. *Nucl. Phys. A* 153:49 (1970)
25. Typel S, Wolter HH. *Few-Body Syst.* 29:75 (2000)
26. Typel S, Baur G. *Ann. Phys.* 305:228 (2003)
27. Aliotta M, et al. *AIP Conf. Proc.* 561:116 (2001)
28. Spitaleri C, et al. *Phys. Rev. C* 63:055801 (2001)
29. Pellegriti MG, et al. *Nucl. Phys. A* 688:543 (2001)
30. Musumarra A, et al. *Phys. Rev. C* 64:068801 (2001)
31. Tumino A, et al. *Nucl. Phys. A* 718:499 (2003)
32. Pizzone RG, et al. *Nucl. Phys. A* 718:496 (2003)
33. Kadyrov AS, Bray I, Mukhamedzhanov AM, Stelbovics T. *Ann. Phys.* 324:1516 (2009)
34. Mukhamedzhanov AM. *Phys. Rev. C* 84:04461 (2011)
35. Mukhamedzhanov AM, Kadyrov AS, Pang DY. *Eur. Phys. J. A* 56:233 (2020)
36. Lane AM, Thomas RG. *Rev. Mod. Phys.* 30:257 (1958)
37. Hussein MS. *Eur. Phys. J. A* 53:100 (2017)
38. Bertulani CA, Hussein MS, Typel S. *Phys. Lett. B* 776:217 (2018)
39. Faddeev LD. *Sov. Phys. JETP* 12:1014 (1961)
40. Mahaux C, Weidenmüller HA. *Shell-Model Approach to Nuclear Reactions*. Amsterdam: North-Holland (1969)
41. La Cognata M, et al. *Astrophys. J.* 777:143 (2013)
42. La Cognata M, et al. *Astrophys. J.* 739:L54 (2011)
43. Mukhamedzhanov AM, et al. *J. Phys. G* 35:014016 (2008)
44. La Cognata M, et al. *Phys. Rev. Lett.* 109:232701 (2012)
45. Mukhamedzhanov AM. *Phys. Rev. C* 84:044616 (2011)
46. La Cognata M, et al. *Astrophys. J.* 723:1512 (2010)
47. Starrfield S, Iliadis C, Hix WR. *Publ. Astron. Soc. Pac.* 128:051001 (2016)
48. Starrfield S, Iliadis C, Hix WR. Thermonuclear processes. In *Classical Novae*, ed. MF Bode, A Evans, pp. 77–101. Cambridge, UK: Cambridge Univ. Press. 2nd ed. (2008)
49. José J, Shore SN. Observational mysteries and theoretical challenges for abundance studies. In *Classical Novae*, ed. MF Bode, A Evans, pp. 121–40. Cambridge, UK: Cambridge Univ. Press. 2nd ed. (2008)
50. José J. *Stellar Explosions: Hydrodynamics and Nucleosynthesis*. Boca Raton, FL: CRC/Taylor and Francis (2016)
51. Hernanz M, et al. *Astrophys. J.* 526:L97 (1999)
52. Hernanz M, José J. Updated prospects for detectability of classical novae with INTEGRAL. In *Proceedings of the 5th INTEGRAL Workshop on the INTEGRAL Universe*, ed. V Schönfelder, G Lichti, C Winkler, pp. 95–98. Noordwijk, Neth.: Eur. Space Agency (2004)

53. Rehm KE, et al. *Phys. Rev. C* 52:R460 (1995)
54. Rehm KE, et al. *Phys. Rev. C* 53:1950 (1996)
55. Graulich JS, et al. *Phys. Rev. C* 63:011302 (2001)
56. Bardayan DW, et al. *Phys. Rev. C* 63:065802 (2001)
57. Murphy ASJ, et al. *Phys. Rev. C* 79:058801 (2009)
58. de Sereville N, et al. *Phys. Rev. C* 79:015801 (2009)
59. Bardayan DW, et al. *Phys. Rev. Lett.* 89:262501 (2002)
60. Beer CE, et al. *Phys. Rev. C* 83:042801 (2011)
61. Kozub RL, et al. *Phys. Rev. C* 71:032801 (2005)
62. La Cognata M, et al. *Phys. Rev. C* 99:034301 (2019)
63. Dalouzy JC, et al. *Phys. Rev. Lett.* 102:162503 (2009)
64. Adekola AS, et al. *Phys. Rev. C* 83:052801 (2011)
65. Bardayan DW, et al. *Phys. Lett. B* 751:311 (2015)
66. Bardayan DW, et al. *Phys. Rev. C* 96:055806 (2017)
67. Cherubini S, et al. *Phys. Rev. C* 92:015805 (2015)
68. Pizzone RG, et al. *Eur. Phys. J. A* 52:24 (2016)
69. La Cognata M, et al. *Astrophys. J.* 846:65 (2017)
70. Bardayan DW, Kozub RL, Smith MS. *Phys. Rev. C* 71:018801 (2005)
71. Cyburt RH, et al. *Astrophys. J. Suppl. Ser.* 189:240 (2010)
72. José J, Hernanz M. *Astrophys. J.* 494:680 (1998)
73. Cyburt R, Fields B, Olive K. *Rev. Mod. Phys.* 88:015004 (2016)
74. Lamia L, et al. *Astrophys. J.* 768:65 (2013)
75. Tumino A, et al. *Phys. Lett. B* 700:111 (2011)
76. Tumino A, et al. *Astrophys. J.* 785:96 (2014)
77. Li C, et al. *Phys. Rev. C* 92:025805 (2015)
78. La Cognata M, et al. *Phys. Rev. C* 72:065802 (2005)
79. Lamia L, et al. *Astron. Astrophys.* 541:A158 (2012)
80. Pizzone RG, et al. *Astrophys. J.* 786:112 (2014)
81. Hou SQ, et al. *Phys. Rev. C* 91:055802 (2015)
82. Barbagallo M, et al. *Phys. Rev. Lett.* 117:152701 (2016)
83. Kawabata T, et al. *Phys. Rev. Lett.* 118:052701 (2017)
84. Lamia L, et al. *Astrophys. J.* 850:175 (2017)
85. Lamia L, et al. *Astrophys. J.* 879:23 (2019)
86. Tumino A, et al. *Eur. Phys. J. A* 27:243 (2006)
87. Pizzone RG, et al. *Phys. Rev. C* 83:045801 (2011)
88. Farinon F, et al. *Nucl. Instrum. Methods Phys. Res. B* 266:4097 (2008)
89. Lamia L, et al. *Phys. Rev. C* 85:025805 (2012)
90. Mazzocco M, et al. *Nucl. Instrum. Methods Phys. Res. B* 317:223 (2013)
91. Chadwich MB, et al. *Nucl. Data Sheets* 112:2887 (2011)
92. Lugaro M, et al. *Astrophys. J.* 615:934 (2004)
93. Cristallo S, et al. *Astron. Astrophys.* 570:46 (2014)
94. Ugalde C, et al. *Phys. Rev. C* 77:035801 (2008)
95. Pizzone RG, et al. *Astrophys. J.* 836:57 (2017)
96. Pizzone RG, et al. *Phys. Rev. C* 87:025805 (2013)
97. Lamia L, et al. *Nuovo Cim. C* 31:423 (2008)
98. Gulino M, et al. *J. Phys. G* 37:125105 (2010)
99. Gulino M, et al. *Phys. Rev. C* 87:012801 (2013)
100. Guardo GL, et al. *Phys. Rev. C* 95:025807 (2017)
101. Guardo GL, et al. *Eur. Phys. J. A* 55:211 (2019)
102. Coon J. *Phys. Rev.* 80:488 (1950)
103. Batchelor RA, Skyrme THR. *Rev. Sci. Instrum.* 26:1037 (1955)
104. Gibbons IH, Macklin RL. *Phys. Rev.* 114:571 (1959)

105. Costello DG, et al. *Nucl. Sci. Eng.* 39:409 (1970)
106. Drosg M, Otuka N. *Evaluation of the absolute angle-dependent differential neutron production cross sections by the reactions* $^{3}H(p,n)^{3}He$, $^{1}H(t,n)^{3}He$, $^{2}H(d,n)^{3}He$, $^{3}H(d,n)^{4}He$, *and* $^{2}H(t,n)^{4}He$ *and of the cross sections of their time-reversed counterparts up to 30 MeV and beyond*. Rep. INDC (AUS)-0019, Int. At. Energy Agency, Vienna (2015)
107. Brune C, et al. *Phys. Rev. C* 60:015801 (1999)
108. Adahchour A, Descouvemont P. *J. Phys. G* 29:395 (2003)
109. Caughlan GR, Fowler WA. *At. Data Nucl. Data Tables* 40:283 (1988)
110. Pizzone RG, et al. *Eur. Phys. J. A* 56:199 (2020)
111. García-Berro E, et al. *Astrophys. J.* 485:765 (1997)
112. Cooper RL, et al. *Astrophys. J.* 702:660 (2009)
113. Becker HW, Kettner KU, Rolfs C, Trautvetter HP. *Z. Phys. A* 303:305 (1981)
114. Aguilera EF, et al. *Phys. Rev. C* 73:064501 (2006)
115. Spillane T, et al. *Phys. Rev. Lett.* 98:122501 (2007)
116. Mazarakis MG, Stephens WE. *Phys. Rev. C* 7:1280 (1973)
117. High MD, Cujec B. *Nucl. Phys. A* 282:181 (1977)
118. Kettner KU, Lorenz-Wirzba H, Rolfs C. *Z. Phys. A* 298:65 (1980)
119. Patterson JR, et al. *Astrophys. J.* 157:367 (1969)
120. Barrón-Palos L, et al. *Nucl. Phys. A* 779:318 (2006)
121. Jiang CL, et al.*Phys. Rev. C* 97:012801(R) (2018)
122. Fruet G, et al. *Phys. Rev. Lett.* 124:192701 (2020)
123. Tan WP, et al. *Phys. Rev. Lett.* 124:192702 (2020)
124. Abegg R, Davis CA. *Phys. Rev. C* 43:6 (1991)
125. Caciolli A, et al. *Nucl. Instrum. Methods Phys. Res. B* 266:1392 (2008)
126. Zickefoose J. *Phys. Rev. C* 97:065806 (2018)
127. Mukhamedzhanov AM, Kadyrov AS, Pang DY. *Phys. Rev. C* 99:064618 (2019)
128. Bonasera A, Natowitz JB. *Phys. Rev. C* 102:061602(R) (2020)
129. Esbensen H, Tang X, Jiang CL. *Phys. Rev. C* 84:064613 (2011)
130. Jiang CL, et al. *Phys. Rev. Lett.* 110:072701 (2013)
131. Godbey K, Simenel C, Umar AS. *Phys. Rev. C* 100:024619 (2019)
132. Zhang N, et al. *Phys. Lett. B* 801:135170 (2020)
133. Tumino A, et al. *Nuovo Cim. C* 42:55 (2019)
134. Pignatari M, et al. *Astrophys. J.* 762:31 (2013)
135. Mori K, et al. *Mon. Not. R. Astron. Soc. Lett.* 482:L70 (2019)
136. Straniero O, Piersanti L, Dominguez I, Tumino A. On the mass of supernova progenitors: the role of the $^{12}C+^{12}C$ reaction. In *Springer Proceedings in Physics*, Vol. 219: *Nuclei in the Cosmos XV*, ed. A Formicola, M Junker, L Gialanella, G Imbriani, pp. 7–11. Cham, Switz.: Springer. **https://doi.org/10.1007/978-3-030-13876-9_2** (2019)
137. Käppeler F, Gallino R, Bisterzo S, Aoki W. *Rev. Mod. Phys.* 83:157 (2011)
138. Adsley P, et al. *Phys. Rev. C* 103:015805 (2021)
139. Mumpower MR, et al. *Prog. Part. Nucl. Phys.* 86:86 (2016)